Quantitative Multi-Slice Cerebral Perfusion Imaging Using Arterial Spin Labelling MR Techniques

Martin Peter Petric, B.Sc.

Medical Physics Unit
McGill University
Montréal, Québec, Canada

A thesis submitted to the Faculty of Graduate Studies and Research in partial fulfillment of the requirements of the degree of Master of Science

---

Abstract

This thesis presents the development and implementation of a quantitative multi-slice cerebral perfusion imaging technique using magnetic resonance imaging. An acquisition sequence capable of acquiring up to 9 slices was designed and implemented into two final pulse sequences: an interleaved perfusion/BOLD (blood oxygenation level dependent) sequence and a perfusion-only sequence. A number of practical imaging issues were addressed and resolved, including the design of an appropriate inversion pulse for labelling of arterial spins, spatial offsetting of this pulse for use in the arterial spin labelling technique chosen for implementation, and the design of various saturation pulses necessary for quantification of the technique. Experimental validation of the quantitative multi-slice perfusion technique was performed by measuring visual cortex cerebral blood flow (CBF) values in a group of 8 subjects using a block-design visual stimulus paradigm. Results indicated good sequence stability and CBF measurements agreed well with quantitative values found in the literature.

Résumé

Cette thèse présente le développement et la mise en place d'une technique multi-coupe quantitative d'imagerie de perfusion cérébrale utilisant l'imagerie par résonance magnétique. Une séquence d'acquisition capable d'enregistrer jusqu'à 9 coupes a été conçue et implémentée dans deux séquences finales de pulsation: une première de perfusion/BOLD (acronyme anglais pour niveau de dépendance d'oxygénation du sang) inter-lames et une seconde de perfusion seule. Plusieurs problèmes pratiques d'imagerie furent discutés et résolus, incluant la conception d'une pulsation d'inversion dédiée à l'étiquetage des spins arteriaux, le décentrage spatial de celle-ci afin de l'utiliser dans la technique d'étiquetage choisie et la conception de diverses pulsations nécessaires à la quantification de cette technique. La validation expérimentale de cette technique a été accomplie grâce à des mesures de débit sanguin cérébral dans le cortex visuel de 8 sujets en utilisant un paradigme de stimulation visuelle en blocs. Les résultats indiquent une bonne stabilité de la séquence et les valeurs de débit sanguin mesurées sont en accord avec les résultats présentés dans la littérature.

Acknowledgements

I would like to thank my supervisor, Dr. G. Bruce Pike, for his support and guidance throughout this project as well as for providing an open and enjoyable environment in the imaging lab. I would also like to convey my warmest thanks to all of my lab mates: Ives Levesque, Najmeh Khalili, Mike Ferreira, Jennifer Campbell, Bojana Stefanovic, Valentina Petre, Dr. Alexander Bastos, Dr. John Sled, Dr. Jeff Atkinson, and especially my close friend, confidant, and coffee partner Marguerite Wieckowska, for making every day in the lab an enjoyable one. My fondest appreciation go to my family for the unwavering encouragement and support they have provided throughout this degree. Lastly, I would like to thank Marie-Laure Camborde for her support and encouragement as well as for her patience and selflessness without which this thesis would not have been possible.

In addition, I would like to acknowledge the financial support I have received from the Natural Sciences and Engineering Research Council of Canada (NSERC) for which I am grateful.

Contents

Glossary of Terms

ADC	analogue-to-digital converter
ASL	arterial spin labelling
BOLD	blood oxygen level dependent
CASL	continuous arterial spin labelling
CBF	cerebral blood flow
CBV	cerebral blood volume
EPI	echo planar imaging
EPISTAR	EPI and signal targeting with alternating radio frequency
FAIR	flow-sensitive alternating inversion recovery
FID	free induction decay
fMRI	functional magnetic resonance imaging
FOV	field-of-view
MNI	Montreal Neurological Institute
MRI	magnetic resonance imaging
MT	magnetization transfer
NMR	nuclear magnetic resonance
PASL	pulses arterial spin labelling
PET	positron emission tomography
PICORE	proximal inversion with control for off-resonance effects
QUIPSS	quantitative imaging of perfusion using a single subtraction
Q2TIPS	QUIPSS II with thin-slice TI_1 periodic saturation
RF	radio frequency
ROI	region-of-interest
SNR	signal-to-noise ratio
SPECT	single photon emission computed tomography
T_1	spin-lattice relaxation constant
T_2	spin-spin relaxation constant
T_2^*	transverse relaxation time
TE	echo time
TR	repetition time

List of Figures

Chapter 1

Introduction

The past decade has been witness to a tremendous number of advances in the field of mapping human brain function. One huge step forward was the development of functional magnetic resonance imaging (fMRI) in 1991. fMRI is performed by repeatedly acquiring a series of images of the brain while some stimulus is presented or a task is performed. Areas in the brain activated by the stimulus or task will show changes in local neuronal and metabolic activity and fMRI sequences are designed to be sensitive to such changes.

The most commonly employed fMRI techniques are based on the detection of blood oxygenation level dependent (BOLD) signal changes in cortical tissue. These techniques take advantage of the differing magnetic properties of oxyhemoglobin and deoxyhemoglobin to detect changes in blood oxygenation in regions of the brain. These methods are based on the hypothesis that neuronal activation is associated with a significant increase in tissue perfusion with little change in the amount of oxygen consumed. Although BOLD fMRI has several advantages over former functional imaging techniques, its problems include the fact that the signal changes detected may be localized to macroscopic veins that can be remote from the activated cortex and the fact that quantification of the BOLD signal is difficult due to its dependence on multiple parameters such as cerebral blood flow (CBF), cerebral blood volume (CBV), vessel size and oxygen consumption rate.

One method which improves upon the information provided by BOLD is perfusion imaging. This imaging technique is performed by acquiring images of the brain with and without the presence of a perfusion tracer and subtracting the images to obtain a map of CBF. Perfusion imaging not only provides measurements of CBF but does so on a microscopic scale by localizing changes to capillaries. The most common methods of perfusion MR imaging use magnetically labelled endogenous water as a

tracer. These methods, known as arterial spin labelling (ASL), are completely non-invasive and have a very good time resolution compared to methods based on exogenous contrast agents.

Although several different methods of ASL perfusion have been developed, most only provide information regarding relative CBF making validation with gold standard CBF measurement methods such as positron emission tomography (PET) difficult. One important reason why these ASL techniques do not provide quantitative measurements of perfusion is that there is a spatially varying delay in the transit of the tracer water from the labelling region to the imaging slice that cannot be measured from a single image subtraction. This problem can be avoided by using various methods to control the time width of the labelled water tracer.

An additional extension of perfusion imaging using MRI is the modification from single-slice to multi-slice image acquisitions in order to increase the spatial coverage of the technique. Concerns which arise when using ASL in these regards are the destructive effects of the image acquisition at one slice on the magnetically labelled water bolus as it flows towards further slices.

The goal of this thesis was to develop and implement a quantitative multi-slice cerebral perfusion imaging sequence using arterial spin labelling magnetic resonance imaging at the Montreal Neurological Institute (MNI). Although successful single-slice, qualitative perfusion imaging sequences using ASL have been implemented at the MNI, a robust multi-slice, quantitative one has not. The resulting sequences should greatly improve the usefulness of these techniques by providing non-invasive methods through which the absolute CBF values over large regions of the brain can be determined.

The thesis consists of six chapters. The second chapter provides a brief review of the basic theory of MRI as well as an overview of the theory of fast imaging and BOLD fMRI. The third chapter consists of a thorough review of the current literature on arterial spin labelling techniques. The sequence design considerations that were encountered during the development and implementation of the quantitative multi-slice perfusion sequences are described in Chapter Four. In Chapter Five experimental results obtained during the validation of the implemented sequences are presented and discussed. Chapter Six brings the thesis to a close with a summary of final conclusions and future work.

Chapter 2

MR Theory

2.1 Nuclear Magnetic Resonance

Magnetic resonance, or nuclear magnetic resonance (NMR) as it was more commonly referred to at the time, was discovered independently by Purcell and Bloch in 1946 [1, 2]. In 1952, both shared the Nobel Prize for Physics for this discovery which would eventually lead to the development of NMR spectroscopy and magnetic resonance imaging (MRI). Although a complete understanding of the NMR phenomenon requires a strong background in quantum mechanics, a classical description is usually sufficient in explaining MRI. As such, the following introduction to the theory of MRI physics will focus mainly on classical descriptions with some quantum mechanical descriptions included where appropriate. For a more complete explanation there are several excellent texts on the subject [3, 4].

The NMR phenomenon arises in atoms that possess an odd number of nucleons. These nuclei have a non-zero angular momentum that can be expressed as:

$$\mathbf{S} = \hbar \mathbf{I} \tag{2.1}$$

where $\hbar$ is Planck's constant divided by 2π and $\mathbf{I}$ is the quantum mechanical spin operator. Classically, these nuclei with non-zero angular momentum can be thought of as spinning charges or more simply as small current loops which generate a magnetic dipole with a dipole moment μ expressed by:

$$\mu = \gamma \mathbf{S} \tag{2.2}$$

where γ is a constant known as the gyromagnetic ratio which is unique for different nuclear species. Nuclei exhibiting the NMR phenomenon include ^{1}H (γ = 42.576 MHz/T), ^{31}P (γ = 17.235 MHz/T), and ^{23}Na (γ = 11.262 MHz/T) [5]. Of these ^{1}H is the most widely used in MRI due to its abundance *in vivo* in biological tissue (in the form of water and fat). Another important quantity that can be defined is the net magnetization of

a sample **M**. The net magnetization is simply the vector sum of all the individual magnetic moments:

$$\mathbf{M} = \sum_i \mu_i. \tag{2.3}$$

When placed in an external magnetic field $\mathbf{B_0}$, a precessional behavior of the magnetization occurs. Classically, this comes about through a torque experienced by the dipole moments given by:

$$\tau = \mu \times \mathbf{B_0}. \tag{2.4}$$

Since, from classical physics, torque is equal to the rate of change of angular momentum:

$$\tau = \frac{d\mathbf{S}}{dt} = \mu \times \mathbf{B}_0. \tag{2.5}$$

Multiplying both sides by γ gives:

$$\frac{d\mu}{dt} = \mu \times \gamma \mathbf{B}_0 \tag{2.6}$$

which describes a precessional motion about the direction of the field $\mathbf{B_0}$ as illustrated in Figure 2.1.

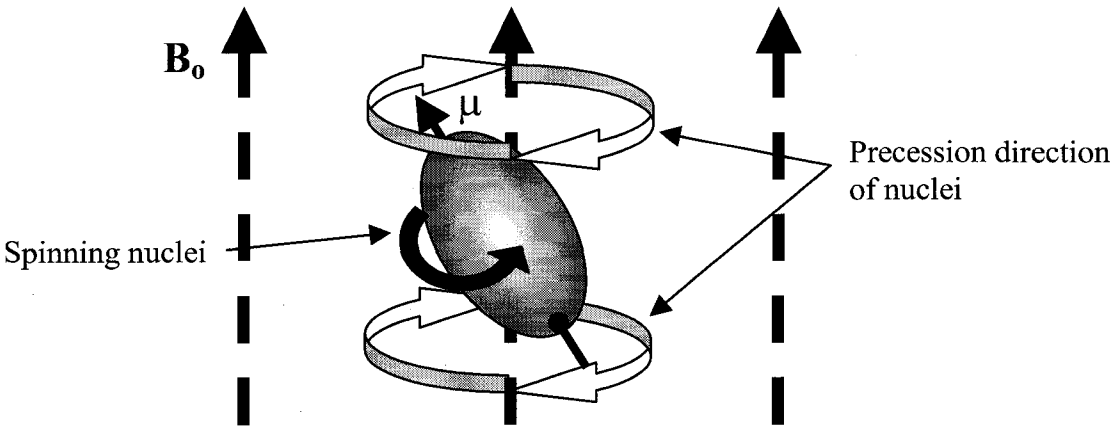

Figure 2.1: Precession of spinning nuclei about the direction of the external magnetic field $\mathbf{B_0}$.

This precessional motion also holds true for the summation of μ or the net magnetization **M** thus:

$$\frac{d\mathbf{M}}{dt} = \mathbf{M} \times \gamma \mathbf{B}_0. \tag{2.7}$$

The frequency of this precession is given by:

$$\omega = \gamma \mathbf{B_o} \quad [\text{rad/s}] \tag{2.8}$$

or conversely:

$$f = \frac{\gamma}{2\pi} \mathbf{B_o} \quad [\text{Hz}] \tag{2.9}$$

where ω is known as the Larmor frequency.

2.2 Excitation

The magnetization of a sample is particularly susceptible to radio-frequency (RF) fields that are in tune with the Larmor frequency. When irradiated with RF energy pulses at this resonance frequency the nuclei efficiently absorb the energy. If an RF pulse $\mathbf{B_1}$ is applied such that it is oriented perpendicularly to $\mathbf{B_o}$ then the net magnetization precesses about the vector sum of $\mathbf{B_o}$ and $\mathbf{B_1}$ and rotates away from the direction of the magnetic field. Since the net magnetization is precessing at the Larmor frequency, this rotation actually occurs through a spiraling motion away from $\mathbf{B_o}$. In order to present a simplified explanation of this motion one can change frames of reference to one that is rotating at the Larmor frequency. Now upon absorption of the energy from the RF pulse, the magnetization simply rotates away from $\mathbf{B_o}$ as shown in Figure 2.2.

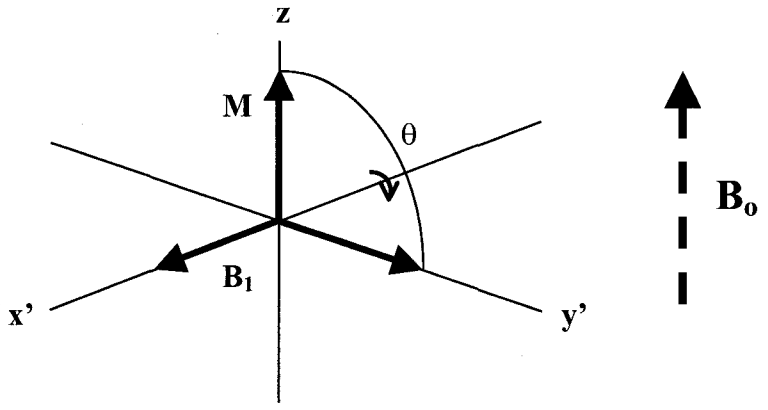

Figure 2.2: From a rotating frame of reference $\mathbf{B_1}$ induces a rotation of the net magnetization about the axis along which it is applied.

The flip angle (θ) through which the net magnetization rotates is determined by both the strength and duration of the RF pulse. Conventionally, $\mathbf{B_o}$ is defined to lie along the z-

axis and RF pulses are oriented perpendicular in the xy plane. The z-axis is commonly referred to as the longitudinal direction while the x and y-axes define what is known as the transverse plane. An excitation where the flip angle is set to 90° thus rotates the net magnetization completely out of the longitudinal direction so that it is lying entirely in the transverse plane. This type of excitation is generally referred to as a saturation pulse. Conversely an excitation with a flip angle of 180° is called an inversion pulse since it rotates the magnetization from the z direction to the –z direction with nothing lying in the transverse plane.

2.3 Relaxation

Relaxation refers to the process of return of the net magnetization to its equilibrium position upon termination of the excitation pulse. The energy that is absorbed during excitation is released during relaxation in the form of electromagnetic waves (RF) and the nuclei regain their original state of alignment in the external magnetic field. There are two relaxation processes which are responsible of this return to the steady state.

T_1 relaxation is the re-growth of the magnetization in the longitudinal direction or M_z. This re-growth, which is also termed spin-lattice relaxation, comes about as excited nuclei lose their energy by transferring it to other molecules. The potential energy of the excited nuclei is transferred to the surrounding lattice through interactions of randomly fluctuating magnetic fields which come about due to motion of surrounding magnetic dipoles. As such, the rate of this relaxation is dependent on the temperature and molecular reorientation frequencies, or correlation times, of the molecules. T_1 relaxation is governed by the first order process:

$$\frac{dM_z}{dt} = -\frac{(M_z - M_o)}{T_1} \tag{2.10}$$

which has the solution:

$$M_z(t) = M_o + [M_z(0) - M_o]\exp\left(-\frac{t}{T_1}\right). \tag{2.11}$$

If the initial excitation was a 90° saturation pulse then this is simplified to:

$$M_z(t) = M_o\left[1 - \exp\left(-\frac{t}{T_1}\right)\right] \tag{2.12}$$

which is an exponential growth equation as demonstrated in Figure 2.3 for a T_1 = 1s.

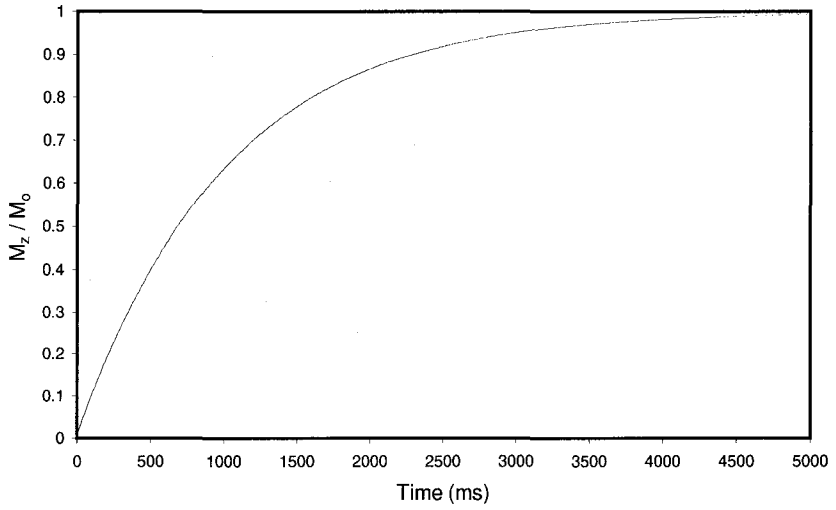

Figure 2.3: Exponential re-growth of M_z due to T_1 relaxation following a saturation pulse. T_1 = 1s.

T_2 relaxation describes the decay of the magnetization in the transverse plane or M_{xy}. This decay is also referred to as spin-spin relaxation and comes about due to nuclear interactions that include the transitions that give rise to T_1 relaxation. In addition to these interactions, the magnetization in the transverse plane is also degraded by de-phasing of the nuclear spins. As a result of nuclei experiencing the fluctuating magnetic fields of their environment nuclei develop slightly different precessional frequencies over space and time. In time, the transverse magnetizations of different nuclei thus become out of phase with each other which leads to a degradation of the net magnetization vector strength in the xy-plane. This de-phasing process is illustrated in Figure 2.4.

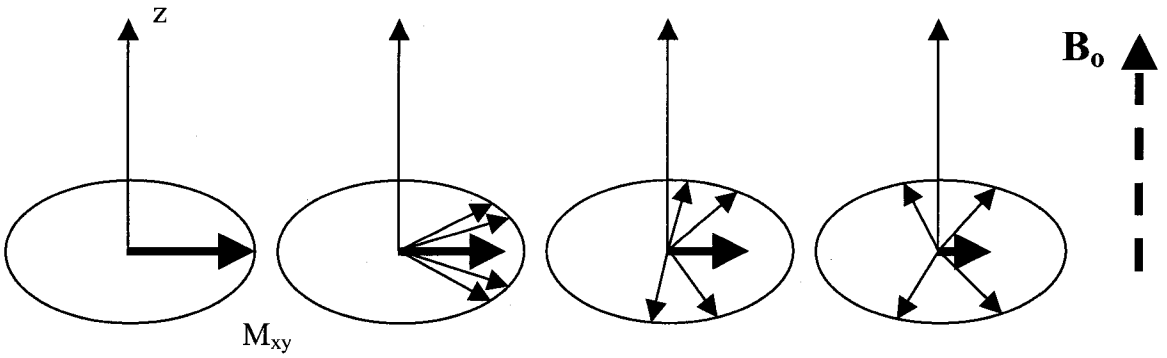

Figure 2.4: Decay of transverse magnetization, M_{xy}, from spin-spin de-phasing following a saturation pulse. The large arrow represents the net transverse magnetization (M_{xy}).

The decay of the transverse magnetization is governed by the equation:

$$\frac{dM_{xy}}{dt} = -\frac{(M_{xy})}{T_2} \tag{2.13}$$

which yields a solution:

$$M_{xy}(t) = M_{xy}(t=0)\exp\left(-\frac{t}{T_2}\right). \tag{2.14}$$

Following a 90° excitation pulse this becomes:

$$M_{xy}(t) = M_o\exp\left(-\frac{t}{T_2}\right) \tag{2.15}$$

which is simply an exponential decay equation. Figure 2.5 illustrates this decay for T_2 = 100ms.

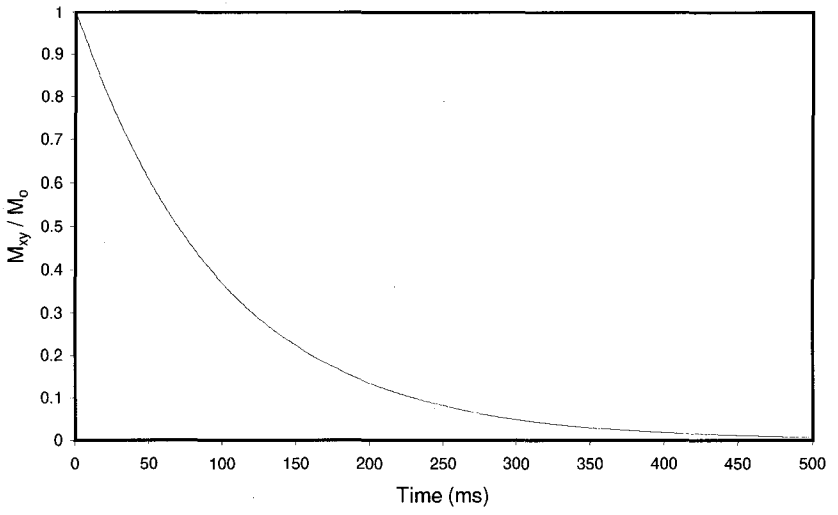

Figure 2.5: Exponential decay of M_{xy} due to T_2 relaxation following a saturation pulse. T_2 = 100ms.

As a result of spin-spin de-phasing, T_1 and T_2 do not have the same value. Typically T_2 is much shorter then T_1 but in all instances $T_2 \leq T_1$.

By combining Equations 2.7, 2.10 and 2.13 one obtains the Bloch equation which describes the evolution of the nuclear magnetization [6]:

$$\frac{d\mathbf{M}}{dt} = \mathbf{M} \times \gamma \mathbf{B} - \frac{M_x \mathbf{i} + M_y \mathbf{j}}{T_2} - \frac{(M_z - M_o)\mathbf{k}}{T_1} \qquad (2.16)$$

where M_o is the sample's equilibrium magnetization due to the B_o field and **i**, **j**, and **k** are unit vectors in the x, y, and z directions respectively.

2.4 Imaging

The process of carrying out a simple NMR experiment can be broken down into three consecutive steps. First the sample of interest is placed in an external magnetic field B_o so that the nuclei align to form a net magnetization vector. Second the sample is irradiated with RF energy at the appropriate resonant frequency to flip the magnetization into the transverse plane. Third the RF irradiation is terminated and the emitted electromagnetic radiation that accompanies relaxation is detected using coils surrounding the sample. The acquisition of an MR image employs the same three basic steps with slight modifications.

A strong super-conducting magnet usually provides the main magnetic field in magnetic resonance imaging. Typically these magnets vary in strength from 0.1 Tesla up to as much as 7 Tesla for human MR imaging. Both the irradiation of the subject with RF energy and the detection of the emitted RF energy are accomplished through the use of RF coils placed in the xy-plane. Several types of RF coils exist and commonly the same coil is used to transmit and receive the RF signals.

A receiving coil acts simply as an antenna. The component of M precessing in the transverse plane changes the flux in the coil and induces an electro-motive force. The current generated by this force is the MR signal, otherwise known as a free induction decay (FID).

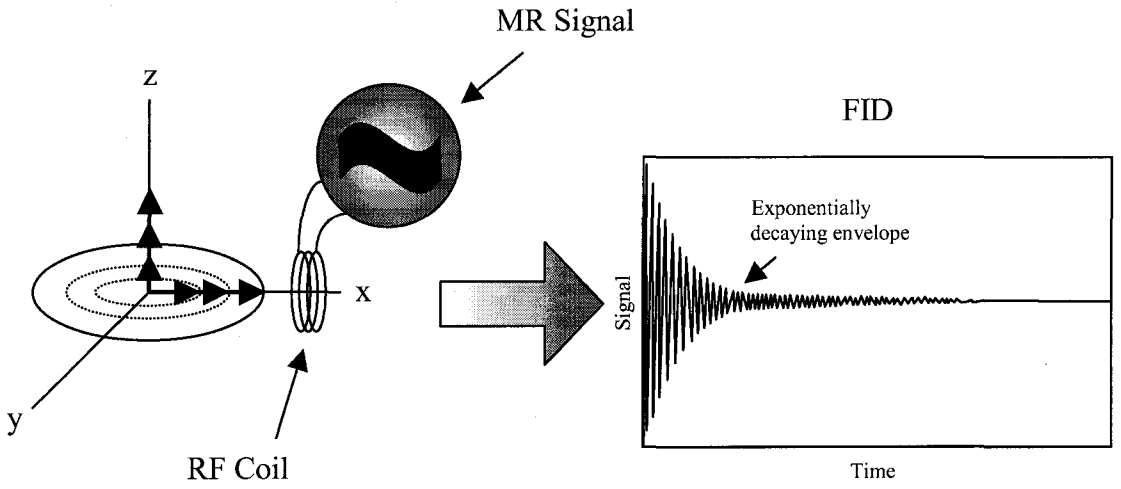

Figure 2.6: Setup of RF receiver coil and free induction decay following an excitation pulse.

As shown in Figure 2.6, the FID consists of a signal with a carrier frequency given by ω which decays in time. The decay of the signal is exponential and has a time constant T_2^* as the magnetization recovers in the longitudinal direction where:

$$\frac{1}{T_2^*} = \frac{1}{T_2} + \frac{1}{T_2'}. \tag{2.17}$$

In an ideal case the decaying envelope would follow an exponential function with time constant T_2. In practice, however, another factor contributes to the de-phasing of the

magnetization in the transverse plane. This de-phasing comes about due to inhomogeneities in the main magnetic field and is the origin of the enhanced rate of M_{xy} decay (T_2' term).

The most important modification to NMR to produce magnetic resonance imaging is the use of linear magnetic field gradients to allow spatial encoding of the MR signal. Each set of gradients varies the z-directed magnetic field strength linearly as a function of one direction. These gradient fields are applied along the three principle directions (x, y, and z) to allow for three-dimensional spatial encoding. The resultant magnetic field strength has a spatial dependence:

$$\mathbf{B}(\mathbf{r}) = (B_o + G_x x + G_y y + G_z z)\,\mathbf{k} \tag{2.18}$$

where G_x, G_y, and G_z are the gradients in the three principle directions. This can also be expressed as:

$$\mathbf{B}(\mathbf{r}) = (B_o + \mathbf{G}\cdot\mathbf{r})\,\mathbf{k} \tag{2.19}$$

where:

$$\mathbf{r} = x\,\mathbf{i} + y\,\mathbf{j} + z\,\mathbf{k} \tag{2.20}$$

and:

$$\mathbf{G} = G_x\mathbf{i} + G_y\mathbf{j} + G_z\mathbf{k}. \tag{2.21}$$

These gradients serve to change the precessional frequencies of the spins at different locations in the sample being scanned so that:

$$\Delta\omega(\mathbf{r}) = \gamma\,\mathbf{G}\cdot\mathbf{r}. \tag{2.22}$$

In this manner, the resonant frequencies at different positions in the sample are unique and are all present in the signal received from the RF receiver coil.

The received signal is the contribution from all of the precessing transverse magnetizations in the volume-of-interest and can be expressed as:

$$s_r(t) = \iiint_{xyz} M(x,y,z,t)\,dxdydz. \tag{2.23}$$

For a set of time-varying magnetic gradients this equation can be expanded to:

$$s_r(t) = \iiint_{xyz} M^{\circ}(x,y,z)\exp\left(-i\gamma\int_0^t \mathbf{G}(\tau)\cdot\mathbf{r}\,d\tau\right)dxdydz \tag{2.24}$$

where M° is the value of M at t = 0 (for simplification two terms have been left out of this expansion: a T_2 relaxation term and an ω_o carrier term). Now if one considers that the

image of interest is simply a 2D function that is based on the integral over the slice width it is useful to express the image as:

$$m(x,y) = \int_{z_0-\Delta z/2}^{z_0+\Delta z/2} M^o(x,y,z)\,dz \tag{2.25}$$

where Δz is the slice thickness. Substituting this equation into Equation 2.24 gives:

$$s(t) = \iint_{xy} m(x,y) e^{-i\gamma\left(\int_0^t G_x(\tau)d\tau\right)x} e^{-i\gamma\left(\int_0^t G_y(\tau)d\tau\right)y} dxdy\,. \tag{2.26}$$

If one now considers the Fourier transform $F(k_x,k_y)$ of a two-dimensional function $f(x,y)$:

$$F(k_x,k_y) = \int_{-\infty}^{\infty}\int_{-\infty}^{\infty} f(x,y) e^{i2\pi(k_x x + k_y y)} dxdy \tag{2.27}$$

and the inverse Fourier transform:

$$f(x,y) = \int_{-\infty}^{\infty}\int_{-\infty}^{\infty} F(k_x,k_y) e^{-i2\pi(k_x x + k_y y)} dk_x dk_y \tag{2.28}$$

it is obvious that m(x,y) is simply the inverse Fourier transform of the signal acquired at any point in time:

$$s(t) = \int_x\int_y m(x,y) e^{-i2\pi[k_x(t)x + k_y(t)y]} dxdy \tag{2.29}$$

where:

$$k_x(t) = \frac{\gamma}{2\pi}\int_0^t G_x(t)d\tau\,, \tag{2.30}$$

$$k_y(t) = \frac{\gamma}{2\pi}\int_0^t G_y(t)d\tau\,. \tag{2.31}$$

Applying the magnetic gradients thus has the effect of moving in spatial frequency, Fourier space, or k-space.

In the formulation above, only the 2D (planar) imaging case was considered. Although three-dimensional image acquisition is possible in MRI, this thesis only deals with two-dimensional acquisitions. In planar imaging the gradient in the z-direction is applied during the excitation step of the procedure. Turning on this slice-selective gradient during excitation limits the participating nuclei to a slice in the z-direction as shown in Figure 2.7.

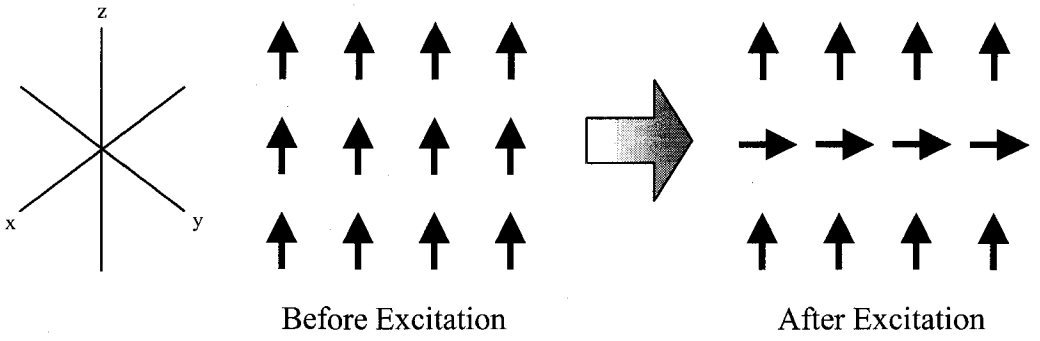

Figure 2.7: Slice selective excitation pulse along the z-direction isolates one dimension of the subject for imaging.

The thickness of the slice defined by the slice-selective excitation depends on both the strength of the magnetic gradient (G_z) and the bandwidth of the excitation pulse employed (BW):

$$\Delta z = \frac{1}{\frac{\gamma}{2\pi} G_z \, BW} \tag{2.32}$$

By using slice selective excitation only one xy-plane of the subject is excited and thereby isolated leaving only two dimensions (x and y) to spatially encode in order to form an image.

Following the slice-selective excitation pulse, standard 2D imaging methods employ a spatial positioning gradient, G_p, which varies linearly in a direction orthogonal to the slice-selection direction. This gradient is left on for a finite period of time thus causing the phases of M_{xy} to vary as a function of spin position in this direction. These differences in phase are known as phase-encoding and the G_p is commonly called the phase-encoding gradient. A short time after phase-encoding is complete the readout of the signal is carried out using the receiver coil and an analogue-to-digital converter (ADC). During readout another spatial positioning gradient, G_r, which is orthogonal to both the slice-selective and the phase-encode directions is engaged. This gradient causes spins along this direction to precess at different frequencies according to their position. Due to these differences in frequency this direction of the subject is said to be frequency-encoded while G_r is known as the readout gradient.

The signal obtained by the receiver coil and the ADC at this point corresponds to a single line in k-space. The strength and duration of each gradient controls the trajectory of this line. Once enough of k-space has been covered, usually through multiple line scanning, the image is reconstructed by taking the 2D inverse Fourier transform of the signal in order find to m(x,y). A typical spin-warp imaging sequence, as the above-described procedure is known, along with its k-space trajectory is depicted in Figure 2.8.

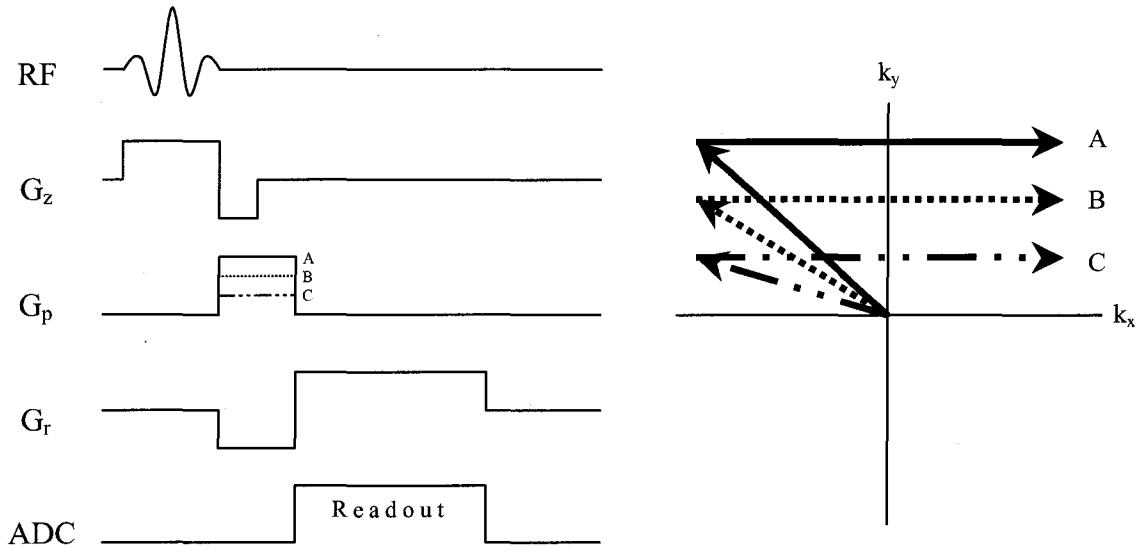

Figure 2.8: A typical spin-warp imaging sequence. Each repetition (A, B, C) with a different G_p strength leads to the acquisition of another line in k-space.

2.5 Fast Imaging

Since the early days of MRI, imaging time has always posed serious practical limitations on this imaging modality. Today a typical high resolution anatomical MRI session usually requires subjects to tolerate lying still inside a scanner for up to an hour. Several different methods of decreasing imaging time have been developed over the years. One application of MRI that benefits greatly from such fast scanning techniques is functional magnetic resonance imaging (fMRI). This application, which will be explained in detail in the following section, benefits greatly from high time resolution of images.

The most common fast imaging technique employed in fMRI is echo planar imaging (EPI). This imaging technique, which was first conceived in 1977 [7], is referred to as a single-shot method since all the data required to reconstruct the image is

acquired following a single excitation pulse. In contrast to the basic spin-warp technique discussed earlier where only a single line in k-space is acquired per readout, EPI is capable of acquiring a sufficient sampling of all of k-space required for image reconstruction in a single readout. Implementation of echo planar imaging sequences requires very strong and fast spatial encoding gradients. These gradients are switched on and off rapidly in order to achieve the necessary k-space trajectory within a time short compared to T_2^*. A typical 2-dimensional echo planar sequence is depicted in Figure 2.9.

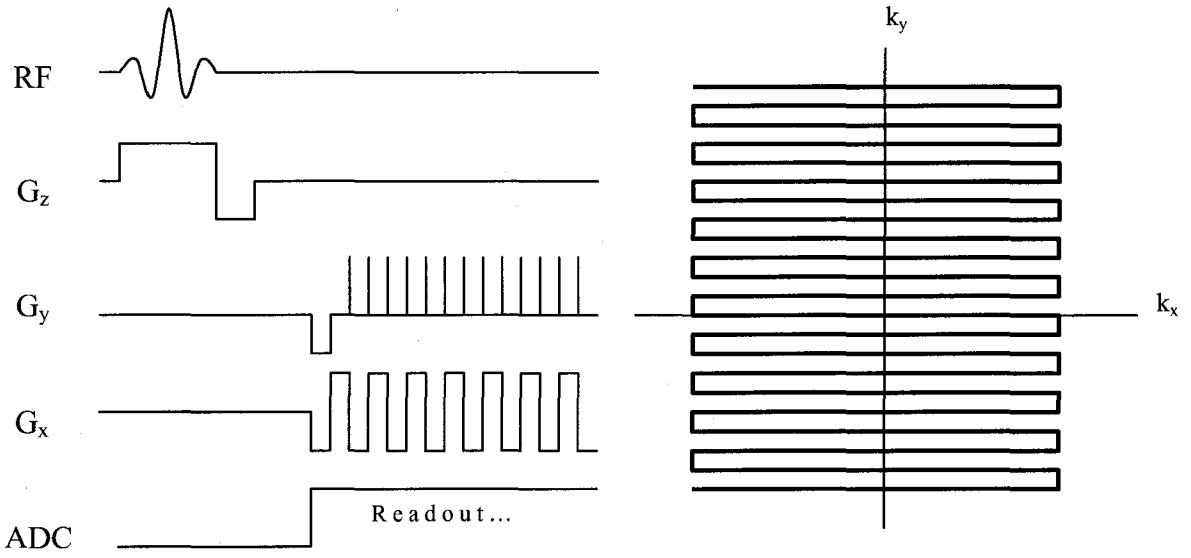

Figure 2.9: A typical 2D echo planar imaging sequence and k-space trajectory. The G_y gradient is blipped along k_y while G_x reads back and forth along k_x.

As shown in the imaging diagram, G_x reads back and forth along parallel lines in k_x while G_y provides blips at the end of each line to move progressively along k_y to provide a Cartesian scan of k-space. Typically a 64 × 64 EPI acquisition takes less than 50 ms thus providing a means by which the motion of an organ or body part can be essentially 'frozen'.

2.6 Functional Brain Imaging

Functional imaging of the human body refers to the acquisition of images that are dependent upon some physiological activity. Although functional imaging is used to acquire physiological information on various parts of the body, functional brain imaging

is a widely investigated field that has lead to the development of several brain-specific functional imaging modalities. Functional brain imaging in man is sometimes referred to as human brain mapping since much of the research in this field has been devoted to investigating the functional importance of the large number of structures which make up the brain.

Traditionally, functional brain imaging is performed primarily through the use of radioactive substances that can be detected in different areas of the brain. The most common of these approaches are single photon emission computed tomography (SPECT) and positron emission tomography (PET). Both of these techniques make use of radioactive tracers that are introduced into the body and localized using radiation detector arrays. PET imaging has several advantages over SPECT which have increased its popularity in functional brain imaging research. These advantages include higher spatial resolution, lower radiation dose to the subject, and a wider range of biologically useful tracer compounds. As a result of the large amount of research that has been performed using PET over the years, this functional imaging modality has become the 'gold standard' method for the measurement of several physiological parameters in the brain including the topic of this thesis, cerebral blood flow (CBF).

Although PET imaging has been responsible for providing a plethora of information on brain physiology, this functional imaging modality has several disadvantages. While superior to SPECT in both regards, spatial resolution in PET is still limited (between 5 and 10 mm depending on the type of detectors used) [8] and the radiation dose to the subject is still significant, thus limiting the number of scans that can be performed on an individual. In addition to these drawbacks, PET imaging is also very expensive. The high cost of PET is a result of the need for positron emitting tracer radioisotopes. The positron emitters typically used in PET have very short half lives (2.07 minutes for ^{15}O and 109.7 minutes for ^{18}F) necessitating the presence of an on-site cyclotron [8].

While MRI has grown to be a dominant presence in anatomical imaging, the use of this technique for imaging brain function has only recently been exploited. The first human brain maps using function magnetic resonance imaging (fMRI) were acquired in 1991 by Belliveau *et al.* [9]. These images were obtained using a cerebral blood volume

technique that followed the passage of a bolus of paramagnetic contrast agent. Since the introduction of fMRI there have been many advancements in this field with the development of several other function MRI imaging methods. The physiological parameters these methods use to infer neuronal activation in the brain include cerebral blood volume (CBV), cerebral blood flow (CBF), and blood oxygenation.

The fMRI method used most commonly today is known as the blood oxygen level dependent (BOLD) method. This method, which was introduced by Ogawa *et al.* [10], uses endogenous deoxyhemoglobin as a contrast agent. BOLD fMRI makes use of the fact that deoxyhemoglobin is paramagnetic while oxyhemoglobin is slightly diamagnetic. As such, the presence of deoxyhemoglobin creates microscopic magnetic field inhomogeneities which serve to enhance the rate of decay of the transverse magnetization. T_2 values for blood at 1.5 T have been found to vary from 30 ms to 250 ms for a range of oxyhemoglobin concentration from 30% to 96% [11]. By employing a sequence with timing parameters chosen to maximize T_2^* differences, BOLD imaging is capable of acquiring oxygenation dependent contrast.

The connection between blood oxygenation and neuronal activity is complex. Rises in the activity of neurons are known to increase the neuronal oxygen demand to meet the demands of ATP-dependant ion pumps present in the neuronal cell membrane [12, 13]. Although this increased metabolism of oxygen leads to the production of more deoxyhemoglobin, the increase in oxygen demand has also been shown to stimulate accelerated tissue perfusion, or blood flow [14, 15]. This increase in local perfusion leads to a dilution of the deoxyhemoglobin as well as a distension of the venous vessels thus increasing CBV. As a result, the net effect is a reduction in the absolute concentration of deoxyhemoglobin leading to an increase in the T_2^*-weighted (BOLD) fMRI signal during brain activation [16, 17].

The dependence of the BOLD signal on CBF, CBV and neuronal oxygen utilization makes quantification of activation a difficult task. In addition, BOLD signal changes occur not only in capillaries but also in macroscopic veins that may be distant to the actual activated region. Several attempts have been made to isolate and quantify the various parameters that constitute the BOLD signal as well as to localize these parameters in terms of microvasculature (capillaries). One promising set of techniques

that address both microscopic activation localization as well as isolation and quantification of cerebral blood flow are perfusion imaging methods. Perfusion imaging can provide a more direct measure of neuronal activity and can be used to study the physiological origins of the BOLD signal.

Chapter 3

Arterial Spin Labelling

3.1 Introduction

Current methodologies used to directly measure cerebral blood flow all make use of tracer kinetic theory in order to arrive at a calculation of CBF. By following a tracer through the brain and applying acquired data to mathematical models of brain perfusion these techniques give an estimate of the cerebral blood flow. The types of tracers used in perfusion imaging studies can be broken up into two main groups: diffusible tracers and non-diffusible tracers. A non-diffusible tracer refers to a compound that remains in the vascular space and does not equilibrate across the blood-brain barrier [18]. Although the use of non-diffusible tracers provides very good sensitivity, this characteristic leads to serious problems in determining absolute blood flow measurements. Some commonly used non-diffusible tracers include ^{131}I-labelled albumin (SPECT imaging) and paramagnetic MR contrasts agents such as gadolinium-DTPA. Alternatively, diffusible tracers readily equilibrate across the blood-brain barrier making absolute measurement of CBF possible. Commonly used diffusible tracers include the positron emitters $H_2{}^{15}O$, ^{133}Xe and ^{14}C-iodoantypirine [19].

In 1992, Detre *et al.* introduced a new method of MR perfusion imaging using magnetically labeled arterial water as a diffusible tracer [20, 21]. In this technique, pre-inversion pulses are used to invert the magnetization of arterial blood slightly upstream from the region-of-interest (ROI). Blood flow carries these magnetically labelled water molecules to the brain imaging voxels of interest where they are transferred from the capillaries to the brain water pool. The experiment is then repeated in the absence of any pre-inversion pulses and the images are subtracted in order to yield a difference image whose intensities are directly related to quantitative local perfusion values. This technique is now commonly referred to as arterial spin labelling or simply ASL.

3.2 Continuous ASL Techniques

The first ASL technique introduced by Detre *et al.* was a continuous arterial spin labelling (CASL) method. Continuous arterial spin labelling techniques magnetically label arterial blood spins as they pass through a plane proximal to the region of interest in the brain. Continuous tagging at this inversion plane is accomplished through the presence of a constant gradient and RF excitation. The resultant continuous flow of tagged arterial blood spins into the region of interest causes the development of a steady state condition identical to the steady state conditions that develop during the use of exogenous contrast agents. A schematic illustrating a simple CASL technique is shown in Figure 3.1.

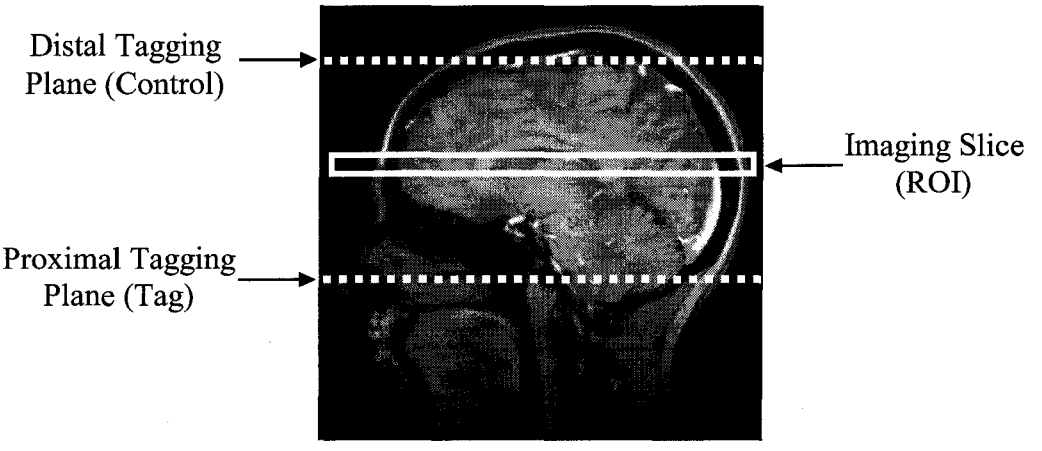

Figure 3.1: A typical CASL schematic representation. The proximal tagging plane, on during the tag acquisition, continuously inverts crossing arterial blood spins while the distal tagging plane, applied during acquisition of control images, cancels out magnetization transfer effects.

As depicted in Figure 3.1, in addition to the proximal tagging plane, most continuous arterial spin labelling techniques also employ a distal tagging plane which is equidistant from the imaging slice during control image acquisition in order to account for magnetization transfer (MT) effects from confounding the difference images. Magnetization transfer effects arise due to the use of off-resonant RF pulses in forming the spatially offset tagging plane. These off-resonant pulses excite macromolecular protons that in turn cause a decrease in signal and in T_1 relaxation values of the measured

water magnetization [22, 23]. Since the off-resonant tagging pulses are not present in the acquisition of the control images, the subsequent image subtraction can lead to large systematic errors that are due to MT effects and are independent of CBF values. The use of a distal tagging plane that is equidistant from the imaging slice during acquisition of the control image eliminates these errors by taking advantage of the fact that MT effects are highly symmetric with frequency [20]. Creating a distal tagging plane by reversing the frequency offset of the proximal RF pulses introduces identical MT effects into both tag and control images. These effects are thus cancelled out during the image subtraction to create perfusion images.

Although continuous arterial spin labelling techniques are successfully used in many centers around the world, these techniques have several disadvantages. The constant RF that is necessary to produce a continuous tagging region has the effect of depositing excessive power into the subject. While human perfusion scans using CASL can be performed within safe energy deposition limits on standard field strength magnets (~1.5 T), this characteristic may limit the use of CASL methods at higher field strength magnets (3+ T) which are now appearing on the market [18]. Another problem with continuous arterial spin labelling techniques arises in the extension of single slice CASL acquisitions to multi-slice acquisitions. In the original CASL technique described above an extension to multi-slice is not possible while still accounting for MT effects since both tagging planes would have to be equidistant from each slice of the acquisition. Solutions to this problem have included using alternate methods to account for MT effects such as employing an amplitude modulated control whereby two inversion planes are created that doubly invert the spins during the control image acquisition. In addition to these disadvantages, certain MRI units are simply incapable of performing continuous labelling due to their hardware configuration not allowing for continuous RF irradiation.

3.3 Pulsed ASL Techniques

Pulsed arterial spin labelling (PASL) methods label large blood volumes using short RF pulses. In this case a specific volume of blood is labelled upstream from the region of interest in contrast to CASL methods which label all blood flowing through a plane upstream from the imaging region. In recent years, PASL techniques have grown in

popularity for two main reasons. Firstly, the short RF pulses used in PASL cause less off-resonance saturation (MT) effects and deposit less power in the subject compared to CASL. Secondly, PASL techniques can be implemented on any MRI unit since the RF pulses required are standard, short duration, volume irradiations.

EPISTAR

One of the first implementations of PASL was carried out by Edelman *et al.* in 1994 [24]. This technique, known as echo-planar imaging and signal targeting with alternating radio frequency (EPISTAR), employs an adiabatic inversion pulse to selectively invert the magnetization of a slab of tissue proximal to the imaging slice. Image acquisition is performed at a time TI following this inversion in order to allow arterial blood from the inversion slab to flow into the imaging slice. The sequence is then repeated with the inversion slab positioned distal to the imaging slice in order to cancel out magnetization transfer effects in a manner similar to that used in CASL. A schematic of the EPISTAR technique is shown is Figure 3.2.

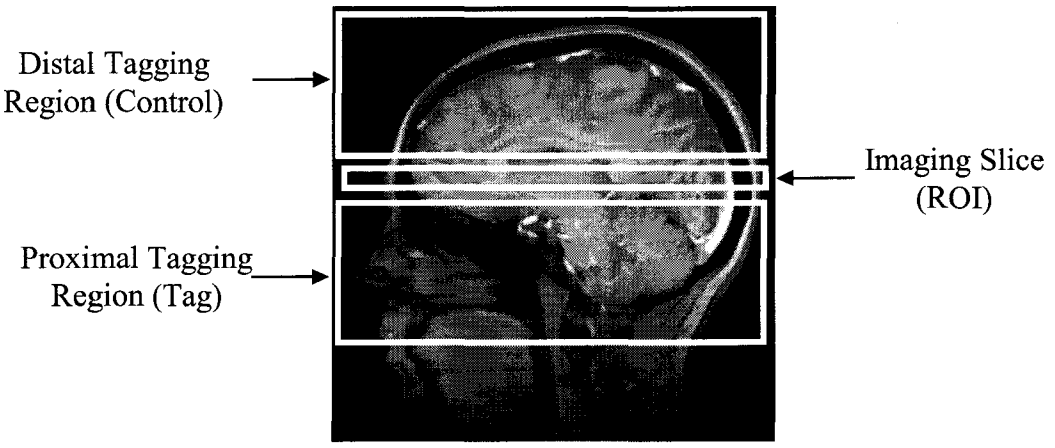

Figure 3.2: A schematic representation of the EPISTAR technique. In the tag acquisition the proximal tagging region inverts a large volume of arterial blood spins while in the control acquisition the distal tagging region serves to cancel out magnetization transfer effects.

Although the EPISTAR method provides a rapid, noninvasive means for creating qualitative maps of CBF, inherent problems with this technique have caused it to slip

from common use. Although the distal control inversion used in EPISTAR eliminates magnetization transfer effects when acquiring image sets centered on isocenter, this is not true for acquisitions where the image set has been shifted in the z-direction. Complete cancellation of the MT effects depends on the tag and control inversions being positioned at equal distances away from the isocenter of the main magnetic field. When the central imaging slice is shifted away from this position, the distances between the isocenter and the tag and control pulses (i.e. the off-resonance frequency of each pulse) are no longer equivalent and MT effects will contribute to the resultant difference images. This complication limits the positioning of the imaged slices making it necessary to physically move the subject in order to accurately position imaged slices in the desired manner. Additionally, the use of the distal control inversion in EPISTAR has been found to lead to visualization of additional veins that have been tagged by the control inversion [24]. These venous signals which flow from distal to proximal confound the difference images upon subtraction.

FAIR

Since its introduction several variations of pulsed arterial spin labelling have been developed. One particularly popular method developed independently by Kwong *et al.* [25] and Kim [26] in 1995 is known as flow-sensitive alternating inversion recovery (FAIR). In the FAIR method the tag image is acquired by applying a slice selective inversion pulse centered on the imaging slice while the control image employs a non-selective inversion which essentially inverts everything. In this case the perfusion contrast comes about from the uninverted blood entering the imaging slice following the selective inversion of the tag image. Magnetization transfer effects are not an issue when using FAIR since both tag and control images are acquired using the same on resonance RF pulse with the only difference being the presence or absence of slice selective gradients. An illustration of the FAIR technique is shown in Figure 3.3.

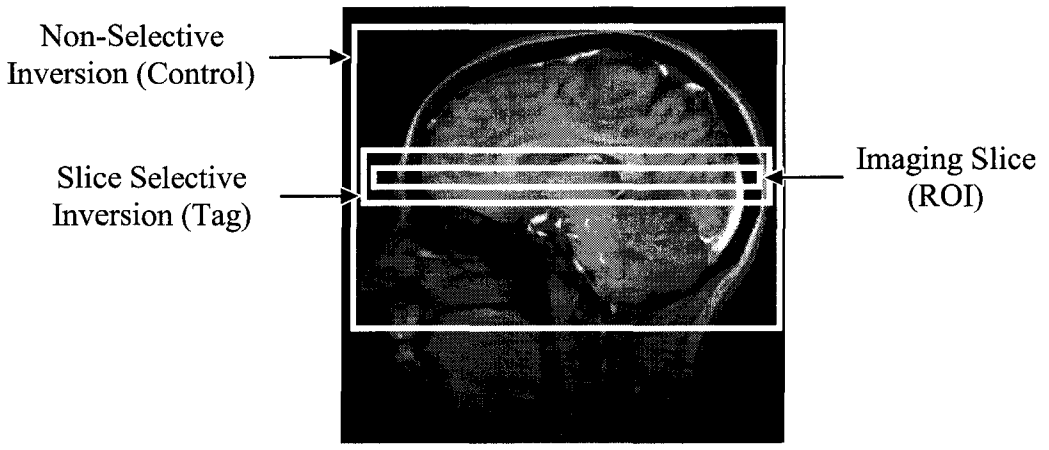

Figure 3.3: Representation of the FAIR technique. A slice selective inversion is applied during the tag acquisition followed by a non-selective inversion during the control. Perfusion contrast now comes about as a result of uninverted arterial blood entering the ROI.

Although the FAIR technique avoids the magnetization transfer issues encountered when performing multi-slice acquisitions using EPISTAR, this method still has the problem of tagged blood entering the imaging slice from the distal side of the slice selective inversion slab. Even worse than EPISTAR where the distally tagged blood appears as negative signal, in FAIR this signal is positive and as such is impossible to differentiate from blood originating proximal to the slice [27].

PICORE

One of the most recent PASL techniques was introduced by Wong *et al.* in 1997 [27]. This method, which is a modification of the original EPISTAR technique, is known as proximal inversion with control for off-resonance effects (PICORE). In PICORE the tag is applied in the same manner as in EPISTAR with an off-resonant adiabatic RF pulse inverting a slab proximal to the imaging region. PICORE differs from EPISTAR in the acquisition of the control image. In PICORE the control image uses the same off-resonant RF pulse but in the absence of a magnetic field gradient thus inverting nothing. Since the same pulse is used in both images, subtraction cancels out any MT effects

completely. Additionally, the fact that the control off-resonant RF pulse inverts nothing means that there is no signal from distal blood entering the imaging region.

3.4 Kinetic Models for ASL Signal

Once MT effects have been accounted for and control and tag images are acquired, the transformation of the subtracted image signal into a quantifiable measurement of cerebral blood flow values depends on mathematical kinetic modeling. Although several kinetic models have been proposed to describe ASL in relation to specific experimental techniques [20, 21, 25, 26, 28], Buxton *et al.* [29] were successful in unifying these theories into general and standard models of the ASL signal for both continuous and pulsed techniques.

The general model of ASL, as derived by Buxton *et al.* [29], applies to both continuous and pulsed ASL techniques. This model comes about by considering that the magnetization difference of a given voxel at a time t depends on three independent functions representing delivery, clearance and longitudinal relaxation of the labelled blood. The delivery of the arterial flow is represented by a delivery function, c(t), which is the normalized concentration of magnetization arriving at the voxel at time t. The clearance of the magnetization by venous flow is represented by a residue function, r(t,t′), which gives the fraction of the labelled spins that arrive at time t′ and remain in the voxel at time t. The longitudinal relaxation of the spins is represented by a magnetization relaxation function, m(t,t′), which gives the fraction of the original tag longitudinal magnetization carried by the spins that arrive at time t′ and remain at time t. Immediately following the inversion pulse the magnetization difference is given by $2\alpha M_{oB}$ where M_{oB} is the equilibrium magnetization of the blood and α represents the inversion efficiency of the labelling pulse. The delivery function enters the equation first as the amount of magnetization delivered to the voxel between t′ and t′ + dt′ is given by $2\alpha M_{oB} f c(t')$ where f is the CBF in milliliters of blood per ml of voxel volume per second. The remaining two functions are added when one considers the fraction of magnetization that remains in the voxel at time t. This is given by:

$$\Delta M(t) = 2\alpha M_{oB} f \int_0^t c(t')r(t-t')m(t-t')dt \quad (3.1)$$

which can alternatively be represented, using the convolution operation, as:

$$\Delta M(t) = 2\alpha M_{oB} f \{c(t) * [r(t)m(t)]\} \quad (3.2)$$

which represents a general kinetic model for the ASL signal.

From this general model three key assumptions can be made in order to arrive at standard models of ASL for both continuous and pulsed methods. The first assumption is that labelled blood arrives via uniform plug flow. As a result of this and the fact that the tag is created a short distance away from the imaging slices, there is an initial time delay, Δt, after inversion in which no labelled blood arrives at the voxels. This assumption also dictates that the plug has a defined width that is usually represented as a time width, τ. The tag thus arrives uniformly at the first imaging slice between $t = \Delta t$ and $t = \Delta t + \tau$. At $t > \Delta t + \tau$ arriving blood is no longer labelled. Given uniform plug flow, the arrival function is only non-zero for the time interval $\Delta t < t < \Delta t + \tau$ where:

$$c(t) = \exp[-t / T_{1B}] \quad (3.3)$$

and T_{1B} is the longitudinal relaxation time of blood.

The second assumption is that the water exchange between tissue and blood can be modeled using single-compartment kinetics. This implies that exchange between sub-compartments within the voxels occurs instantaneously such that their concentration ratios are constant despite the change in total tissue concentration with time. As a result of this, the total tissue concentration and the venous concentration are related by a constant ratio equal to the tissue/blood partition coefficient of water, λ, and the residue function can be expressed as:

$$r(t) = \exp[-f t / \lambda]. \quad (3.4)$$

The final assumption for the development of the standard models is that while the magnetization initially decays with the relaxation time of blood, T_{1B}, after reaching the tissue voxel the magnetization takes on the relaxation time of tissue, T_{1t}. This assumption implies the complete extraction of the water from the vascular space immediately after arrival and enables the expansion of the magnetization relaxation function to:

$$m(t) = \exp[-t / T_{1t}]. \tag{3.5}$$

With these three assumptions in place, Equations 3.3, 3.4 and 3.5 can be substituted into Equation 3.2 yielding a standard solution for pulsed ASL methods given by:

$$\Delta M(t) = \begin{cases} 0 & 0 < t < \Delta t \\ 2\alpha M_{oB} f (t - \Delta t) e^{-t/T_{1B}} q(T_{1B}, T_{1t}, T_{ex}, f, \lambda, t) & \Delta t < t < \Delta t + \tau \\ 2\alpha M_{oB} f \tau e^{-t/T_{1B}} q(T_{1B}, T_{1t}, T_{ex}, f, \lambda, t) & \Delta t + \tau < t \end{cases} \tag{3.6}$$

where f is given in milliliters of blood per milliliter of tissue per minute. The term q is a dimensionless correction factor that accounts for the shift in T_1 as the blood is exchanged into brain tissue as well as for the clearance of the tag by outflow. In practice the effects accounted for by q are relatively small and as such q is very close to unity. The standard continuous ASL solution is very similar to the pulsed model. It is given by:

$$\Delta M(t) = \begin{cases} 0 & 0 < t < \Delta t \\ 2\alpha M_{oB} f T_1' e^{-\Delta t/T_{1B}} q(T_{1B}, T_{1t}, T_{ex}, f, \lambda, t) & \Delta t < t < \Delta t + \tau \\ 2\alpha M_{oB} f T_1' e^{-\Delta t/T_{1B}} e^{-(t-\tau-\Delta t)/T_1'} q(T_{1B}, T_{1t}, T_{ex}, f, \lambda, t) & \Delta t + \tau < t \end{cases} \tag{3.7}$$

where:

$$\frac{1}{T_1'} = \frac{1}{T_{1t}} + \frac{f}{\lambda}. \tag{3.8}$$

3.5 Quantification of ASL Measurements

From Equations 3.6 and 3.7 it is apparent that isolating the cerebral blood flow, f, requires knowledge of several parameters. The most troublesome of these are by far the transit delay, Δt, and the time width of the tag, τ. Although direct experimental determination of these parameters is possible by using a minimum of two inversion times, this endeavor at the very minimum doubles the scanning time necessary for acquisition of a complete perfusion data set using a single inversion time. As a result of this, several methods have been proposed in order to decrease or eliminate the dependence of the ASL signal on these parameters.

Quantitative CASL

For continuous ASL techniques, the most effective method for dealing with the variability of Δt and τ is through the introduction of a delay after the application of the inversion tag and before image acquisition as suggested by Alsop and Detre [30] and Ye *et al.* [31]. This delay allows for complete delivery of the inverted blood to the imaging slices thus minimizing the effects of variable transit delays. In addition, this time delay also allows for the passage of arterial blood destined for regions beyond the imaging slices without contribution to the measured ASL signal. Although this technique is routinely and successfully used in centers performing quantitative CASL, it has certain inherent disadvantages. The most obvious drawback to introducing a delay between inversion and image acquisition is the significant reduction in signal amplitude that results from spin relaxation. This effect, along with the relatively poor tagging efficiency inherent to multi-slice CASL, has the expense of decreasing the SNR to values that are comparable to standard usage of pulsed arterial spin labelling methods thus eliminating one of the major benefits of employing CASL [32].

QUIPSS and QUIPSS II

Attempts at quantification of pulsed arterial spin labelling methods have included tedious subject by subject measurement of transit delay parameters [33] as well as application of a time delay identical to that introduced in quantitative CASL techniques [34]. Although these attempts have had some success, the most promising quantitative PASL technique thus far is a method proposed by Wong *et al.* in 1997 [27, 35]. This method has been coined quantitative imaging of perfusion using a single subtraction (QUIPSS) and is applicable to most PASL techniques. In the original QUIPSS implementation (which used a PICORE base sequence), a saturation is applied to the imaging region at a time TI_1 after the tagging inversion pulse. This saturation, which is applied in both the tag and control images, serves to cut off the front end of the tag thereby removing from the difference signal any tagged blood that has arrived prior to TI_1. Image acquisition is carried out at a time TI_2 such that the difference signal arises only from the tagged blood entering the imaging region between TI_1 and TI_2. If the saturation pulse is applied after

the front of the tag has entered the imaging region and image acquisition takes place before the end of tag has entered this region such that:

$$TI_1 > \Delta t \tag{3.9}$$

$$TI_2 < \Delta t + \tau \tag{3.10}$$

then Equation 3.6 simplifies to:

$$\Delta M(TI_2) = 2M_{oB} f \Delta TI e^{-TI_2/T_{1B}} q(T_{1B}, T_{1t}, T_{ex}, f, \lambda, TI_2) \tag{3.11}$$

where:

$$\Delta TI = TI_2 - TI_1. \tag{3.12}$$

Since TI_1 and TI_2 are chosen by the experimenter, determining a quantitative value for CBF is a relatively simple matter using Equation 3.11.

An alternative method to the one detailed above was also proposed in the original QUIPSS paper from Wong *et al.* [27]. This extension is identical to the QUIPSS method and is simply known as QUIPSS II. In QUIPSS II the saturation pulse is applied to the tagging region at time TI_1 as opposed to the imaging slice region. The effect of this saturation pulse is to cut off the end of the tag producing a tagged region that possesses a sharply defined time width, TI_1. If the saturation pulse is applied before the tag leaves the tagging region and the image acquisition is carried out after the end of the tag has entered the imaging region:

$$TI_1 < \tau \tag{3.13}$$

$$TI_2 > TI_1 + \Delta t \tag{3.14}$$

which now simplifies Equation 3.6 to:

$$\Delta M(TI_2) = 2M_{oB} f TI_1 e^{-TI_2/T_{1B}} q(T_{1B}, T_{1t}, T_{ex}, f, \lambda, TI_2). \tag{3.15}$$

This second edition of QUIPSS has several advantages over the original QUIPSS sequence. One of the most important of these is the fact that it is possible to extend the QUIPSS II technique to multi-slice imaging while this is not the case with QUIPSS. In QUIPSS the saturation of the imaging slice at TI_1 destroys the tagged magnetization that will eventually perfuse into further slices making multi-slice image acquisition impossible. Conversely, in QUIPSS II the saturation is applied to the tagging region so the tag remains intact for more distal slices. In addition to this benefit, QUIPSS II has been found to be more accurate in quantitatively determining CBF values then QUIPSS

[35]. This advantage stems from the fact that the signal in the original QUIPSS is primarily intravascular as a result of image acquisition taking place immediately after the end of the bolus enters the imaging slice. The QUIPSS II method allows more time for blood distribution thus avoiding the artifacts caused by imaging blood that is simply passing through the imaging slice bound for more distal tissue.

Q2TIPS

Although QUIPSS II effectively eliminates the dependence of the ASL signal on Δt and τ and provides a multi-slice, quantitative perfusion technique, there are two sources of residual error which can confound the CBF results obtained using this method. These errors stem from: a) incomplete saturation of the tagging region by the QUIPSS II saturation pulse; and b) mismatch of the distal edge of the saturation and inversion slice profiles. Both of these errors come about as a result of the different types of RF pulses used for inversion and saturation in QUIPSS II. As previously mentioned, the inversion pulse used in most PASL techniques, including QUIPSS II, consists of an adiabatic RF pulse. This type of RF pulse is known to have very sharp profile edges as well as excellent inversion efficiency in the presence of B_1 inhomogeneity in the RF coil [36]. Unfortunately, adiabatic pulses cannot be used for magnetization saturations and the pulses used for the saturation of the tagging region in QUIPSS II is accomplished using an ordinary apodized sinc pulse with duller profile edges and efficiency issues due to B_1 inhomogeneity. The ineffectiveness of this saturation pulse causes part of the saturated tag region to contribute to the perfusion signal thus causing an overestimation of the measured CBF and confounding the quantification scheme.

A recent modification to the QUIPSS II method, designed to correct for these problems, has been suggested by Luh *et al.* [37]. This method is known as QUIPSS II with thin-slice TI_1 periodic saturation (Q2TIPS). Q2TIPS improves upon the characteristics of the saturation pulse by replacing it with a train of periodic saturations that are much thinner and briefer than the original QUIPSS II saturation pulse. The slice profiles that result from thin slice sinc pulses are known to have sharper edges as well as improved flip efficiency in the presence of B_1 homogeneities compared to thick slice sinc pulses. In Q2TIPS the periodic saturation train is initiated at a time TI_1 following the

inversion and it is terminated at a time TI_{1S}. The images are then acquired at a time TI_2 and calculation of the cerebral blood flow is carried out as in QUIPSS II. Figure 3.5 shows an illustration of the tagging, presaturation, and imaging regions in a Q2TIPS technique applied to a PICORE pulsed ASL method.

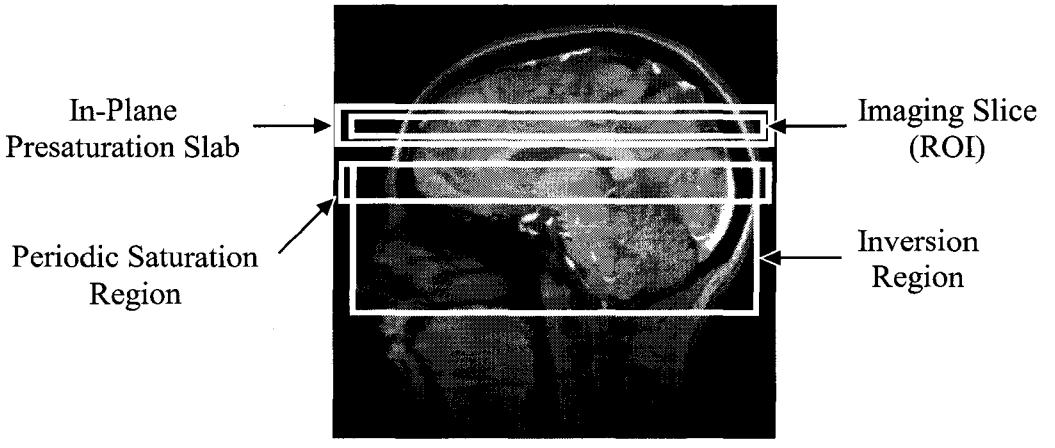

Figure 3.4: Representation of the Q2TIPS technique applied to PICORE. The QUIPSS II saturation pulse has been replaced by a train of thin slice, periodic saturation pulses applied at the distal edge of the hyperbolic secant inversion region.

The corresponding pulse sequence diagram for this method is illustrated in Figure 3.6. Both Figures 3.5 and 3.6 show the tagging acquisition only. As with all PICORE implementations the control acquisition is identical except that the hyperbolic secant pulse is applied in the absence of any gradient thus inverting nothing.

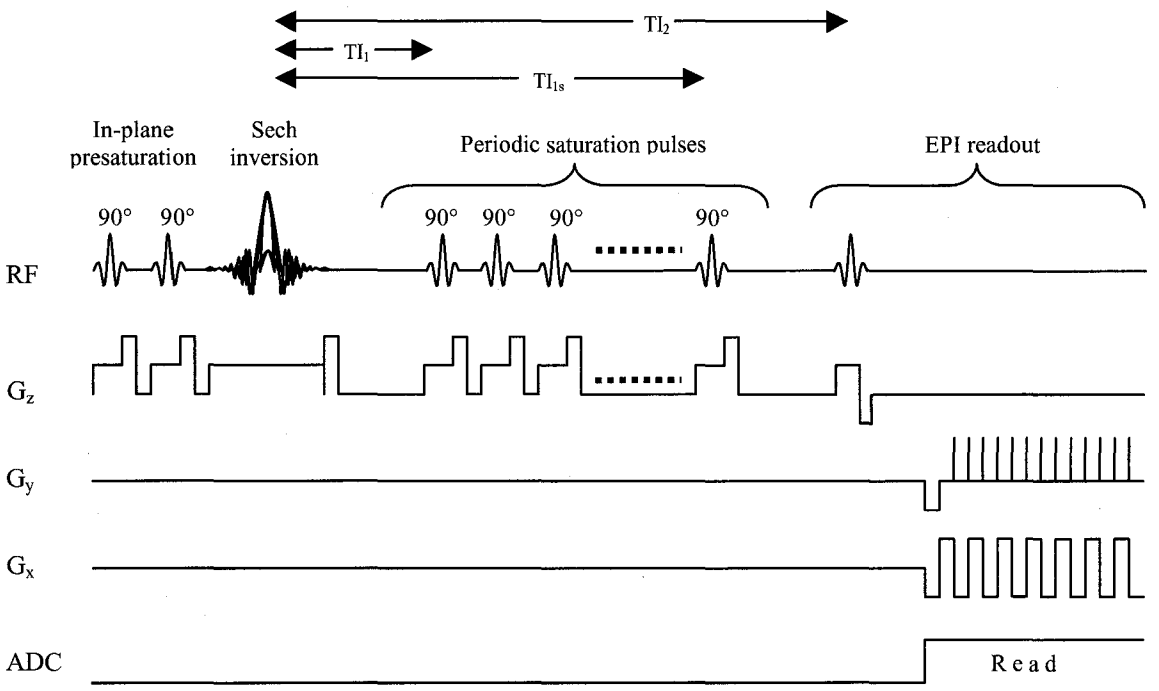

Figure 3.5: Q2TIPS/PICORE pulse sequence diagram [37]. In-plane presaturation pulses precede the spatially offset inversion pulse. Periodic saturation pulses follow at a time TI_1 and last until TI_{1S}. The control schematic is identical except for the absence of the G_z gradient during the inversion pulse.

Luh *et al.* have shown that Q2TIPS is successful in improving the accuracy of quantitative perfusion imaging using both single and multi-slice acquisitions.

Chapter 4

Sequence Design Considerations

Upon evaluation of the recent literature on quantitative ASL methods, it was decided that a multi-slice PICORE/Q2TIPS technique be implemented. In this chapter the major design issues entailed in implementing such a technique are considered. These include development of an appropriate inversion pulse, spatial offsetting of the inversion pulse for use in the PICORE method, and development of both presaturation and Q2TIPS saturation pulses. Each of these issues is discussed in turn with a brief description of the underlying theory, a review of the solutions proposed in the literature, and a presentation and discussion of our own experimental findings.

4.1 Inversion Pulse Development

THEORY

By far the most important step in implementing any quantitative ASL sequence is the design and development of the inversion pulse used for tagging in-flowing arterial spins. The changes in the MR signal intensity between images acquired following arterial inversion and those acquired without inversion are typically on the order of 1 % [18]. Since these changes are so small, quantitative ASL techniques are inherently susceptible to small variations in static tissue signal between the tag and control acquisitions. Such variations come about as a result of imperfections in the slice profile of the inversion pulse used for tagging. Figure 4.1 shows the effects of the inversion slice profile schematically for a 5-slice PICORE perfusion technique.

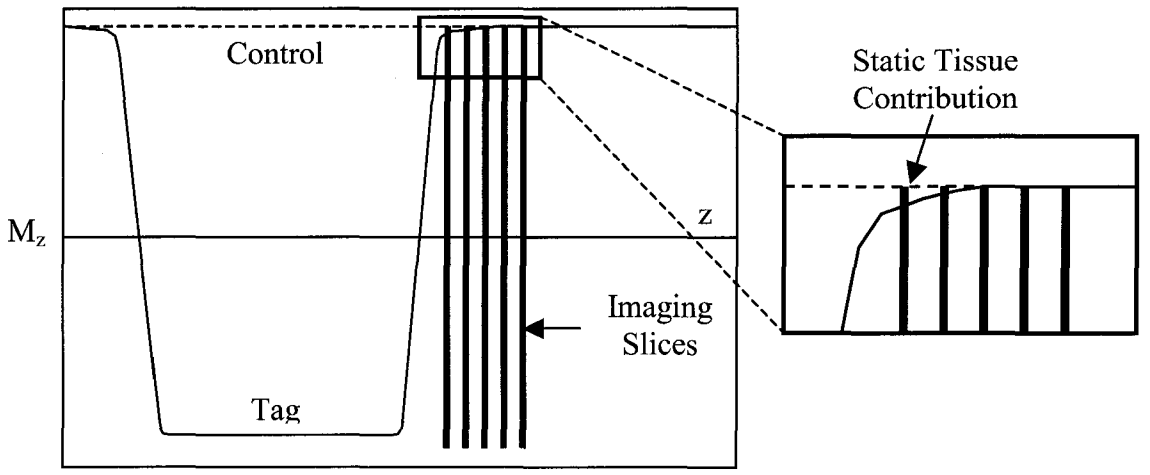

Figure 4.1: Inversion slice profile effects for the PICORE technique [38]. The dashed line represents the control profile while the tag profile is shown as a solid line. A 5-slice acquisition is illustrated here. The inset shows a zoomed view of how slice profile imperfections cause varying static tissue contributions at each slice.

Optimally, Figure 4.1 should show no difference between the tag and control states in the region of the imaging slices. As a result of slice profile imperfections this is not the case. From slice to slice and even across individual slices these imperfections lead to static tissue contributions which can confound the interpretation of the perfusion data. In order to minimize this problem it is crucial that an inversion pulse with a sharply defined profile is used for arterial tagging.

Most pulsed ASL methods make use of hyperbolic secant adiabatic inversion pulses for tagging. As mentioned previously, these inversion pulses are known to have sharp profile edges and excellent inversion efficiency despite the presence of B_1 inhomogeneities. Hyperbolic secant inversion pulses are both amplitude and phase modulated and can be generated using the Silver-Hoult equation [36]:

$$B_1(t) = B_{1o}(\mathrm{sech}(\beta t))^{1+i\mu} \tag{4.1}$$

where μ is a real constant known as the side-to-width parameter and β is measured in s^{-1}. The inversion bandwidth in Hz is then given by:

$$BW = \frac{\mu\beta}{\pi}. \tag{4.2}$$

Another useful way of expressing Equation 4.1 is in terms of a real amplitude pulse:

$$B_1(t) = \text{sech}(\beta t)\,, \tag{4.3}$$

with a frequency modulation:

$$\Delta\omega(t) = -\mu\beta\,\tanh(\beta t)\,. \tag{4.4}$$

The choice of the parameters μ and β is crucial in determining the characteristics of the resultant inversion pulse. Increasing the value of μ has the effect of yielding squarer inversion pulse profiles [36] while at the same time requiring lower transmitter voltages (lower power) to achieve inversion [39]. From Equation 4.2 it is evident that increasing μ also has the effect of decreasing β for a given bandwidth. Unfortunately, as observed in Equation 4.3, reducing the value of β increases the width of the B_1 envelope along with the risk of truncation artifacts at the beginning and end of the pulse [40]. As a result of the interaction of these parameters, the choice of μ and β becomes an optimization problem wherein one attempts to maximize μ while minimizing the degree of truncation of the B_1 envelope.

EXPERIMENTAL FINDINGS

Optimization of the inversion pulse profile was carried out in a manner identical to that used by Payne *et al.* in a study evaluating the use of frequency offset corrected inversion adiabatic pulses [40]. The maximum allowed truncation of the B_1 envelope was set to be approximately 0.4 % of the maximum amplitude:

$$\text{sech}\left(\frac{\beta T_p}{2}\right) \approx 0.4\% \tag{4.5}$$

where T_p is the time length of the pulse. This resulted in β values of 1600 s^{-1}, 800 s^{-1}, and 400 s^{-1} for pulses of length 7.68 ms, 15.36 ms, and 30.72 ms respectively. Optimization of the hyperbolic secant inversion was performed by systematically testing combinations of β values, along with their corresponding T_p values, and μ values. Tests were performed using both an RF pulse simulator and by measuring inversion profiles in a uniform flood phantom.

All RF pulses were created with MATLAB (Version 5.2, The Math Works Inc., Massachusetts, USA) using Equation 4.1. RF simulations were performed on the resultant waveforms using a toolbox designed for use with MATLAB called RF Tools (J

Pauly, Stanford University, 1995). The simulator provided in RF Tools makes use of the Shinnar-Le Roux selective excitation pulse design algorithm [41] in order to compute and plot slice profiles for input RF pulses. Actual visualization of the inversion pulse profiles was accomplished using a Siemens flood phantom doped with $NiSO_4$ ($T_1 \cong 300$ ms). The waveforms for each pulse were first incorporated into an external RF file using GENPULSE, a Siemens software tool which creates RF data files readable by the Magnetom Vision system (Siemens Medical Systems, Erlangen, Germany). Pulse sequences were then designed using a Siemens program called PARGEN (PARameter GENerator) with each experimental inversion pulse oriented perpendicular to the imaging plane. Following an inversion time set to null inverted spins (212 ms for Siemens phantom) a single-shot image was acquired. Profile analysis was performed using an in-house image display utility called XDISP (Version 4.3.5, GB Pike, 2000). An image of the phantom acquired with the single-shot acquisition but in the absence of any inversion pulses is shown in Figure 4.2.

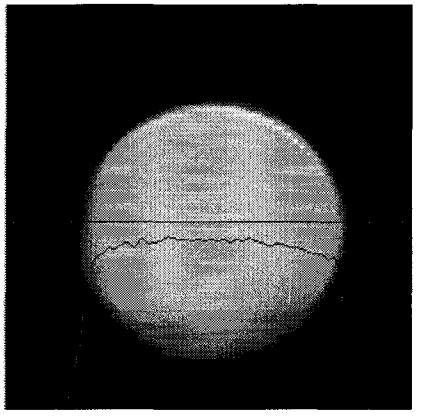

Figure 4.2: Transverse cross-section of Siemens flood phantom acquired with single-shot acquisition used for analysis of inversion profiles. The lower red line shows the profile across the center of the section when no inversion pulse is used.

Optimization of the hyperbolic secant parameters began by testing the effects of μ on the slice profile for a constant value of β and T_p. Initially these parameters were set to the values used in the initial implementation of Q2TIPS by Luh *et al.* with $\beta = 800\ s^{-1}$ and

T_p = 15.36 ms [37]. Figure 4.3 displays the hyperbolic secant functions using these settings with representative values of μ.

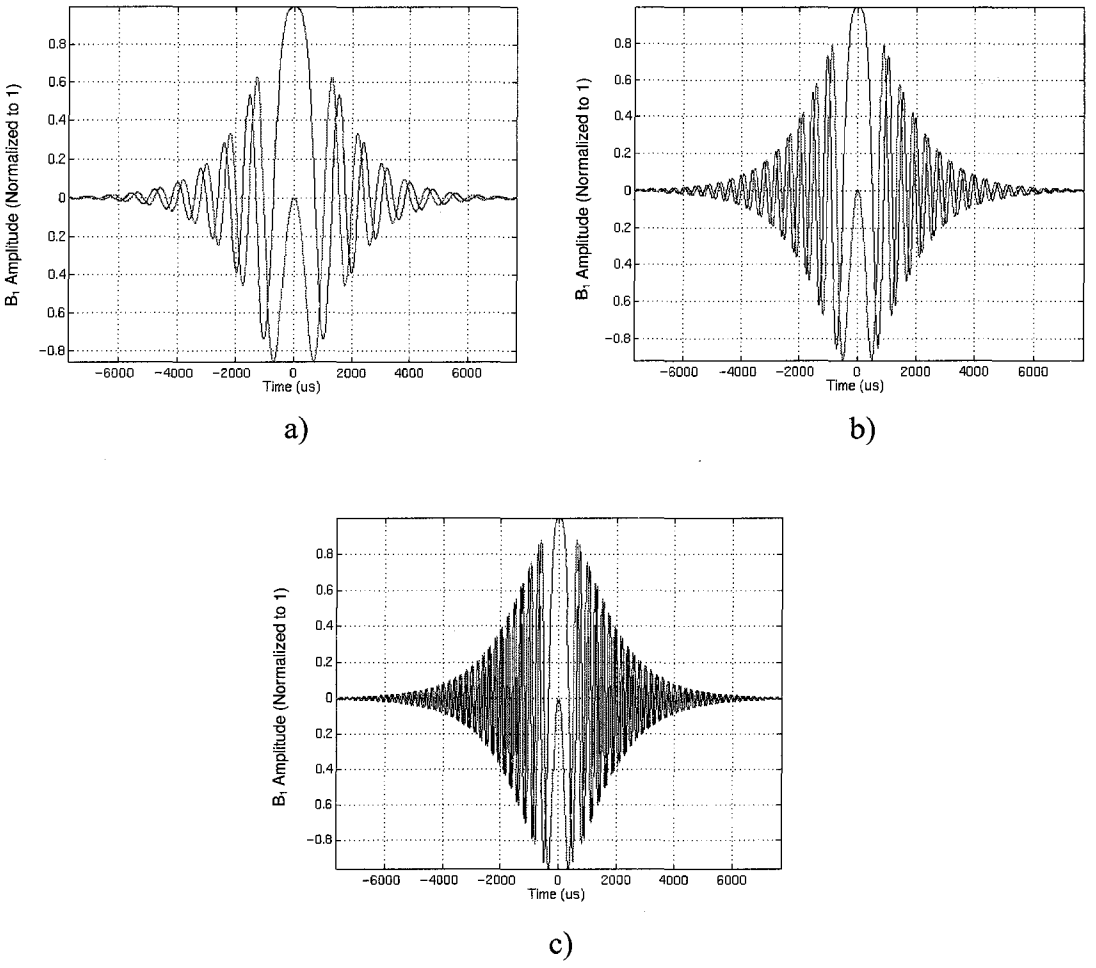

Figure 4.3: Plots of hyperbolic secant functions with μ values of a) 10, b) 20, and c) 40. In all cases β = 800 s^{-1} and T_p = 15.36 ms. The real part of the curves is represented by the blue line while the imaginary part is represented by the red line.

This figure illustrates the general shape of the hyperbolic secant function and how this shape changes with the parameter μ. A profile analysis was carried out for values of μ ranging from 5 to 60. The simulated profiles from this analysis are shown in Figure 4.4.

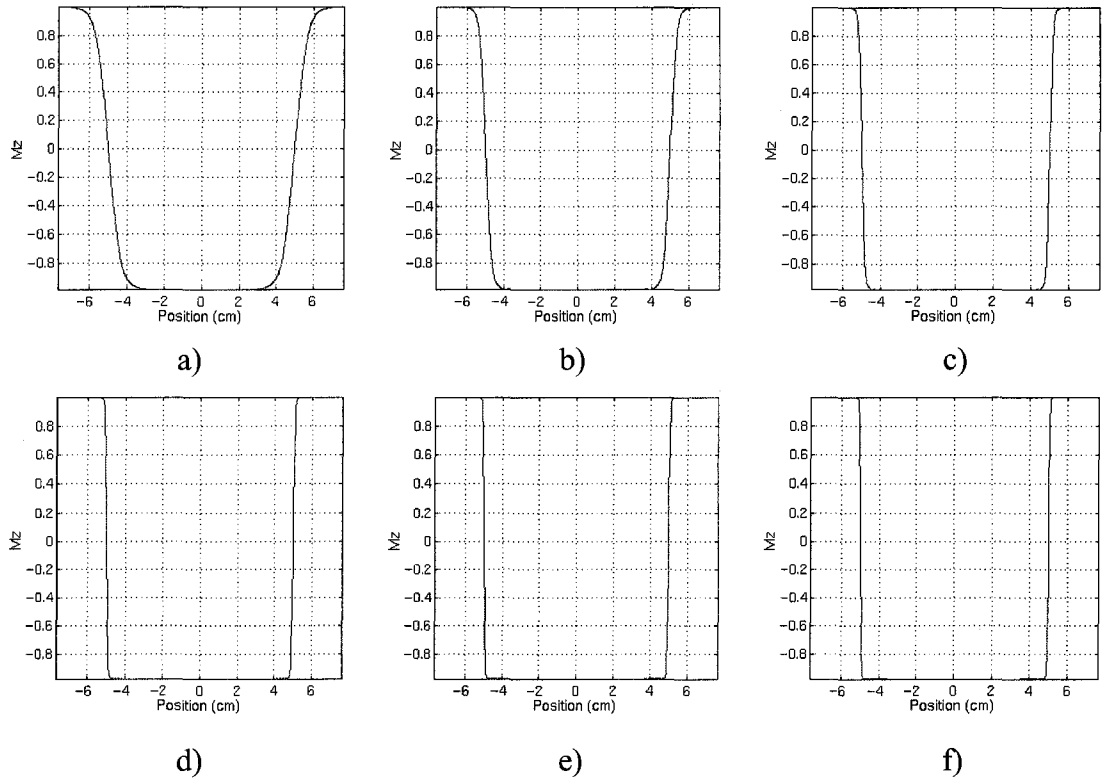

Figure 4.4: Hyperbolic secant inversion profiles from MATLAB RF simulator for β = 800 s^{-1}, T_p = 15.36 ms, and slice thickness = 10 cm. Values of μ are a) 5, b) 10, c) 20, d) 40, e) 50, and f) 60.

Analysis of the simulated profiles indicated no improvement for values of μ greater than 40. The corresponding phantom profiles for these pulses are shown in Figure 4.5.

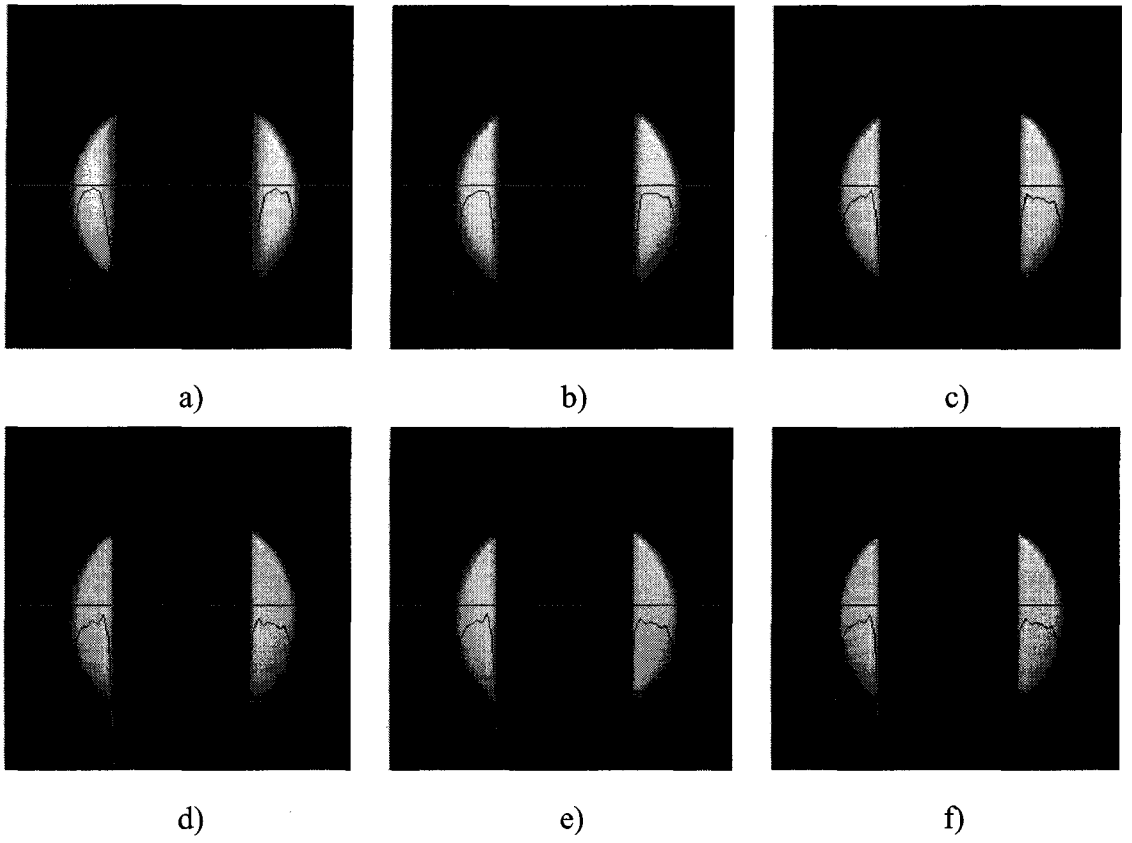

Figure 4.5: Hyperbolic secant inversion images and profiles from a uniform flood phantom for $\beta = 800\ s^{-1}$, $T_p = 15.36$ ms, and slice thickness = 10 cm. Values of μ are a) 5, b) 10, c) 20, d) 40, e) 50, and f) 60.

The in-phantom profiles led to the same conclusion as the simulator profiles: increasing μ beyond 40 has little effect on improving the inversion slice profile. The cause of this cutoff in the improvement of the profile with μ is most likely due to undersampling of the hyperbolic secant function at high μ-values. This undersampling can be predicted by examining the change in the plotted functions in Figure 4.3. When μ exceeds approximately 40, the number of points defining the function (i.e. the time resolution of the RF waveform) is not sufficient to adequately sample the phase changes in the function. This causes additional increases in the side-to-width parameter to be ineffective at improving the shape of the inversion profile.

The effects of the parameter β on the inversion characteristics were investigated by varying β and T_p, in accordance with Equation 4.5, while keeping μ constant at 20. The RF simulator and phantom profile results from these pulses are shown in Figure 4.6.

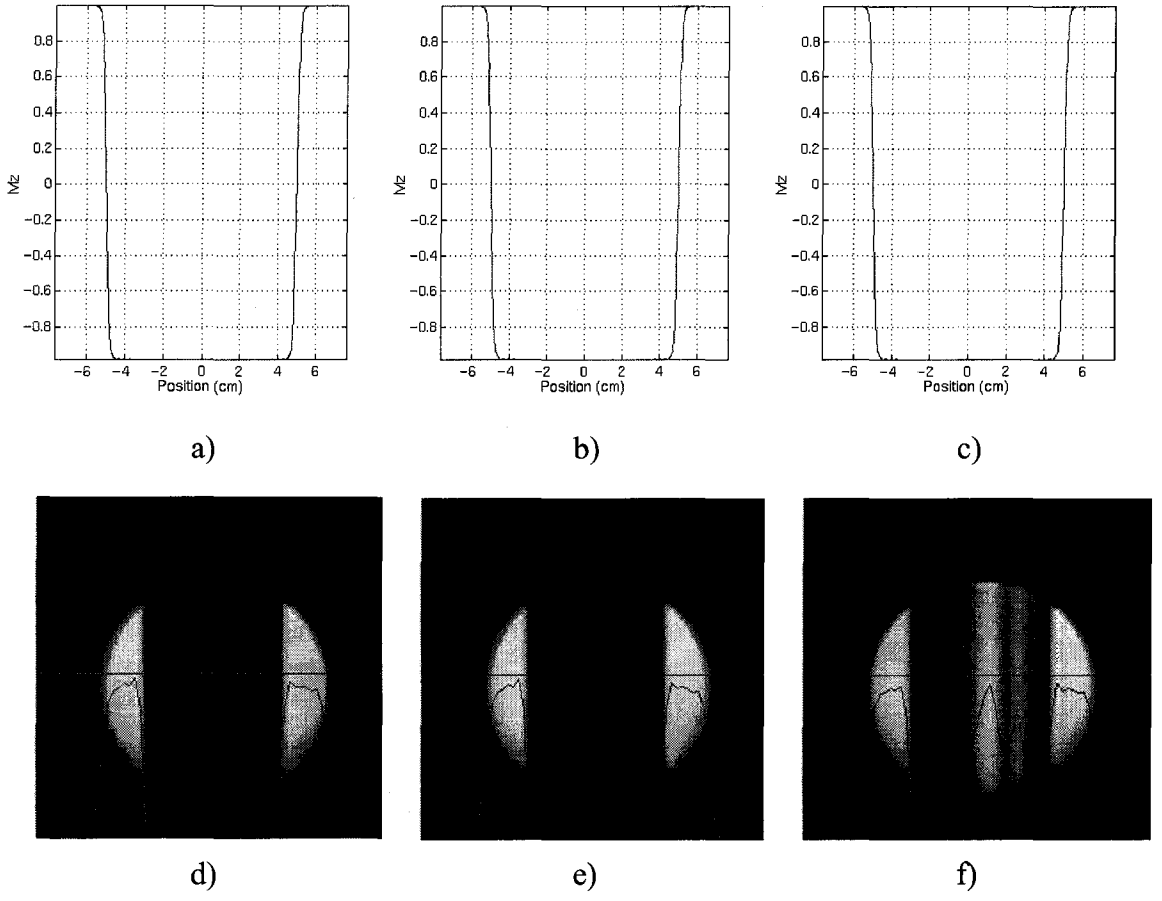

Figure 4.6: Simulator and flood phantom profiles for $\mu = 20$ and slice thickness = 10 cm. Values of β and T_p were varied with $\beta = 400\ s^{-1}$, $T_p = 30.72$ ms for a) and d), $\beta = 800\ s^{-1}$, $T_p = 15.36$ ms for b) and e), and $\beta = 1600\ s^{-1}$, $T_p = 7.68$ ms for c) and f).

As observed in Figure 4.6, no difference is observed between using β values of 400 s^{-1} and 800 s^{-1}. A difference is observed, however, when the value of β is increased to 1600 s^{-1}. At this value the hyperbolic secant pulse is ineffective at uniformly inverting the desired slice resulting in a terrible slice profile. The ineffectiveness of this pulse in inverting the uniform flood phantom is due to the short pulse time necessary to satisfy Equation 4.5. In practice, adiabatic hyperbolic secant pulses invert spins within their bandwidth by sweeping through the respective frequencies. The pulse time of 7.68 ms used when $\beta = 800\ s^{-1}$ is simply too short to accommodate this frequency sweep resulting in inconsistent flip angles along the frequency encoding direction of the slice.

Based on the findings of both the RF simulations and the flood phantom profile tests, optimized values for the inversion pulse were chosen to be $\beta = 800\ s^{-1}$, $\mu = 40$, and $T_p = 15.36$ ms.

4.2 Spatial Offsetting of Inversion Pulse

THEORY

As described earlier, implementation of a PICORE arterial spin labelling technique entails the use of a spatially offset adiabatic inversion pulse in order to invert a slab proximal to the imaging region. In the original PICORE implementation by Wong *et al.*, a 10 cm inversion pulse was employed [21]. This pulse was spatially offset such that a 1 cm gap existed between the distal end of the tagging region and the proximal edge of the most inferior imaging slice. The purpose of this gap was to further reduce the effects of inversion slice profile imperfections on static tissue subtractions. In order to spatially offset the adiabatic inversion pulse the carrier frequency of the pulse was shifted off resonance. The relationship between the spatial offset and the shift in the carrier frequency is given by:

$$\Delta x = \frac{\Delta\omega}{\gamma \cdot G_s} \tag{4.6}$$

where Δx is the spatial offset, $\Delta\omega$ is the shift in carrier frequency, $\gamma = 42.576$ MHz/T and G_s is the slice selection gradient strength in mT/m. This relationship is illustrated in Figure 4.7.

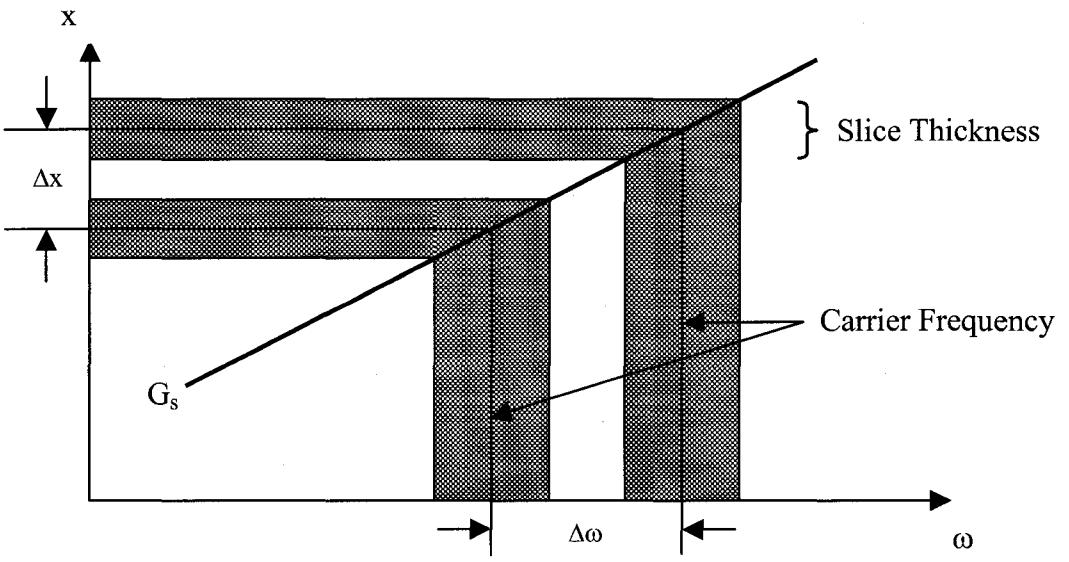

Figure 4.7: Effect of shifting RF pulse carrier frequency on spatial position. In the presence of a magnetic field gradient (thick line), whose slope is determined by G_s, a linear shift of the carrier frequency results in a scaled shift in the spatial position of the pulse.

Practical implementation of this spatial offset is accomplished by multiplying the pulse by a linear phase factor:

$$B_1^{offset}(t) = B_1(t)\, e^{-i\Delta\omega t}. \qquad (4.7)$$

During acquisition of the tag image, this off-resonant inversion pulse is applied in the presence of appropriate magnetic field gradients as specified by the slice thickness and orientation in order to magnetically label spins upstream from the region of interest. During acquisition of the control image the inversion pulse is applied in the absence of any magnetic field gradients thus inverting no spins.

EXPERIMENTAL FINDINGS

Initially, spatial offsetting of the inversion pulse was accomplished by multiplying the phase component of the RF waveform by a linear phase factor calculated for a given offset. This waveform multiplication was performed using MATLAB and the resultant pulses were tested using both the RF simulator and the Siemens flood phantom. Results from these tests are displayed in Figure 4.8.

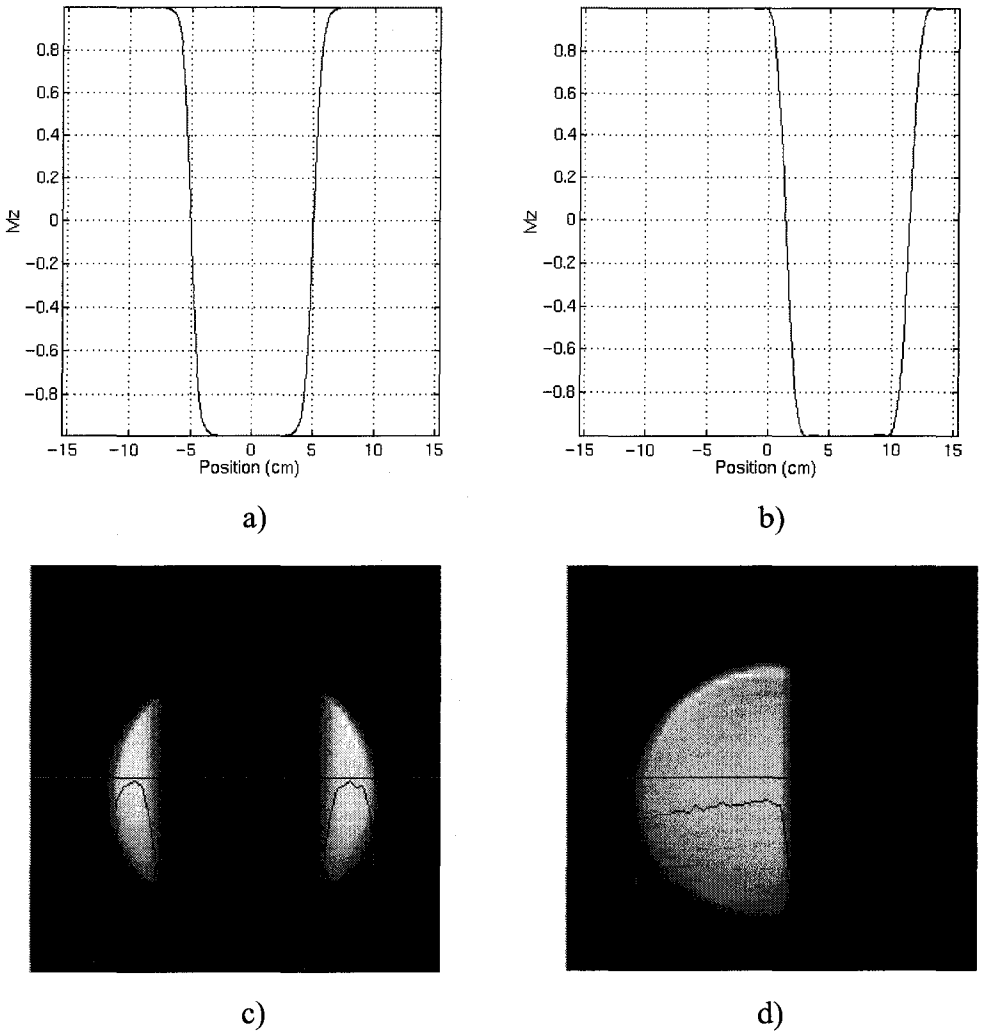

Figure 4.8: Simulator and flood phantom profiles for a hyperbolic secant inversion pulse with $\beta = 800\ s^{-1}$, $\mu = 5$, and $T_p = 15.36$ ms. The effect of the frequency offset on position is illustrated in b) and d) for a spatial offset of 64 mm.

The pulse shown in Figure 4.8 b and d has a center-to-center offset of 64 mm corresponding to the offset necessary for a single-slice acquisition with a slice thickness of 8 mm [21]:

$$\text{Offset} = \frac{\text{Slice Thickness}}{2} + \text{Gap} + \frac{\text{Tag Region Thickness}}{2}. \qquad (4.8)$$

Although this technique of offsetting the inversion pulse worked well in preliminary tests, it was found to have serious limitations upon application in a full

PICORE acquisition. Firstly, the use of this technique of offsetting the inversion pulse does not allow for adjustment of the offset from the console of an MR unit. The shift of the carrier frequency is 'hard-coded' into the RF waveform and thus the inversion region cannot be moved relative to the position of the imaging slice. From Equation 4.8 it is evident that a change in slice thickness directly effects the necessary offset. As a result it is not possible for the user to change slice thickness without loading another inversion pulse with a different spatial offset. This problem is even more serious when one considers multi-slice acquisitions where the offset is given by:

$$\text{Offset} = \frac{[\text{Slice Thickness} \times \text{Number Slices}] + [\text{Slice Separation} \times (\text{Number Slices} - 1)]}{2} \ldots$$

$$+ \text{Gap} + \frac{\text{Tag Region Thickness}}{2}. \qquad (4.9)$$

In this case, the user cannot alter the number of slices, the slice separation or the slice thickness without coding a specific inversion pulse for the exact settings. The second limitation imposed by using this offsetting technique is in fact present at all times when using PICORE arterial spin labelling. This limitation restricts placement of the imaging slices to regions proximal to the isocenter of the magnet. This restriction comes about as a result of the means by which the control images are acquired. As mentioned above, the control images are acquired by playing out the frequency offset hyperbolic secant inversion pulse with no gradients present. As long as the inversion pulse is off resonance no spins are inverted. The problem arises when the imaging slices are positioned too far distal to the isocenter of the magnet. As one moves the slices distally, at some point the inversion pulse bandwidth will begin to overlap with the resonant frequency. When this occurs the control pulse with no gradients will become a non-selective inversion thus inverting all spins. The allowed distal translation before this occurs depends on the offset of the inversion pulse which, from Equation 4.9, depends on the details of the acquisition. In order to allow imaging of superior areas of the brain this limitation had to be overcome. This was accomplished by simply positioning each subject "low" in the magnet. While subjects were positioned normally in the RF head coil, the alignment laser that determines which part of the coil and head will be at isocenter was positioned such that the majority of the head and coil would be positioned proximal to isocenter. In

doing this, imaging of even the most superior parts of the brain became possible using the PICORE technique.

Although the "hard-coded" inversion offset technique described above provided a feasible method of spatially offsetting the inversion pulse another superior technique was eventually chosen for this task. This method makes use of the regional saturation pulse option available on the Siemens Magnetom Vision operating system. The regional saturation pulse option allows the user to input on-resonance external RF waveforms and manipulate their positions directly on the MR console. In this case the MR operating system frequency offsets the inversion pulse according the position chosen by the user. Choice of the position is conveniently provided through a graphical user interface whereby the user drags the region up or down on a scout or anatomical which indicates the position of the brain. An illustration of this user interface is shown in Figure 4.9.

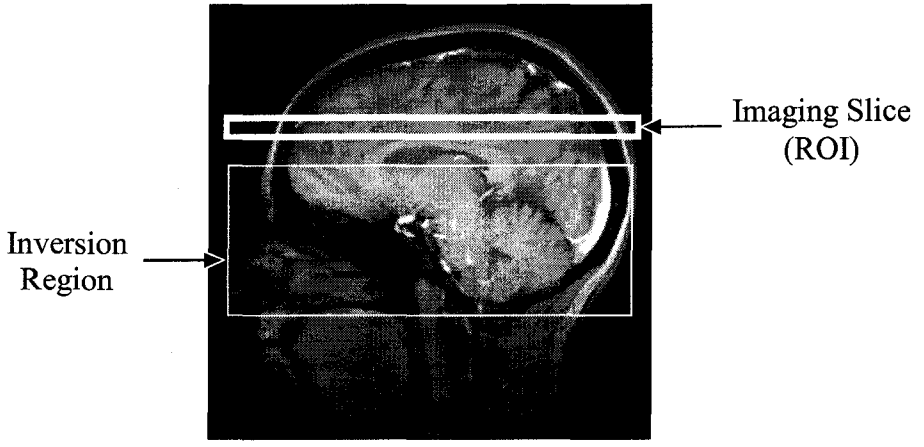

Figure 4.9: Siemens regional saturation pulse graphical user interface for positioning of external RF pulses. The user is free to translate and rotate both the imaging slice and the inversion region with the use of the console mouse prior to scanning.

Although this method seems far superior to the "hard-coded" method, one inherent problem had to be overcome before this offsetting technique could be implemented. The problem with using the regional saturation method comes from acquisition of the control images in PICORE. The regional saturation software computes the necessary frequency offset for the chosen spatial offset using Equation 4.6. Although this works for the tagging acquisitions where the slice selective gradient is present, it

poses a problem for the control acquisitions where there are no gradients present. In this case G_s from Equation 4.6 is equal to zero and the calculated frequency offset will thus be zero despite the user having defined a spatial offset. This problem was overcome rather serendipitously. By chance, a mistake was made during definition of the external RF pulses in the PARGEN code and only a single entry was made for the hyperbolic secant inversion pulse despite the documentation stating that a separate entry must exist for every specific RF pulse-gradient strength combination. Also by chance, the control inversion with no gradients was played out first in the sequence code. This combination of circumstances unintentionally led to the same frequency offset being applied to both pulses with the value of G_s corresponding to the tag inversion. It was later experimentally determined that this was not the case if the tag image was acquired first or if both RF pulse-gradient strength combinations were defined separately. The regional saturation software was inadvertently "tricked" into performing the desired calculation for both inversion pulses. While this solution was effective it is obviously not ideal. However, with a new version of the pulse programming environment soon to be installed, this problem will be corrected via a "legitimate scheme".

Through use of the regional saturation method with this slight modification, the final implementation of the PICORE method was made to be completely user-adjustable with respect to all acquisition parameters appearing in Equation 4.9.

4.3 Presaturation and Q2TIPS Saturation Pulse Development

THEORY

Following development of a spatially offset hyperbolic secant inversion pulse, attempts were made to create a qualitative PICORE sequence by simply placing tag and control inversions in front of single-shot EPI acquisitions. These attempts were found to be unsuccessful at detecting changes in the regional cerebral blood flow. Similar problems were reported in the original implementation of the EPISTAR technique [24] as well as in all implementations of QUIPSS and Q2TIPS [27, 35, 37]. In all cases, the use of presaturation pulses applied to the imaging region immediately prior to the hyperbolic secant inversion pulses were found to improve the detection of regional CBF changes. These pulses extended slightly beyond the imaging slices (~ 4 mm on each side) and

served to further minimize the interaction between the inversion tag and the static tissue in the imaging region.

During development and testing of the presaturation pulse for PICORE, a Q2TIPS saturation pulse was also developed for use in the final quantitative ASL sequence implementation. In the original development of Q2TIPS, Luh *et al.* employed a 3.2 ms three-lobe sinc pulse with a thickness of 2 cm for the purpose of periodically saturating the distal edge of the tagging region [37]. This is a common saturation pulse and was chosen following a brief profile analysis that showed it had a better profile than the 10 cm saturation pulse used in the QUIPSS II technique.

EXPERIMENTAL FINDINGS

Saturation pulses were designed using the RF Tools toolbox. In addition to the aforementioned RF pulse simulator, this toolbox also contains software which uses the Shinnar-Le Roux selective excitation pulse design algorithm for designing RF pulses of various types [41]. Several presaturation and Q2TIPS saturation pulses were created using this software. Pulse profile analysis was carried out using both the MATLAB RF pulse simulator and the uniform flood phantom as described previously.

Selection of the optimum presaturation pulse was based on the need for good slice profile characteristics over a large range of slice thicknesses. This requirement comes about due to the variability of the imaging region with parameters such as the imaging slice thickness, slice separation and number of slices. As these parameters increase so does the imaging region over which the presaturation pulse must extend. In the end, the presaturation pulse chosen was an RF Tools designed 9-lobe least squares filtered sinc pulse with a duration of 2.56 ms. Figure 4.10 shows both the simulated and phantom profiles of this pulse compared to those for a standard Siemens presaturation pulse.

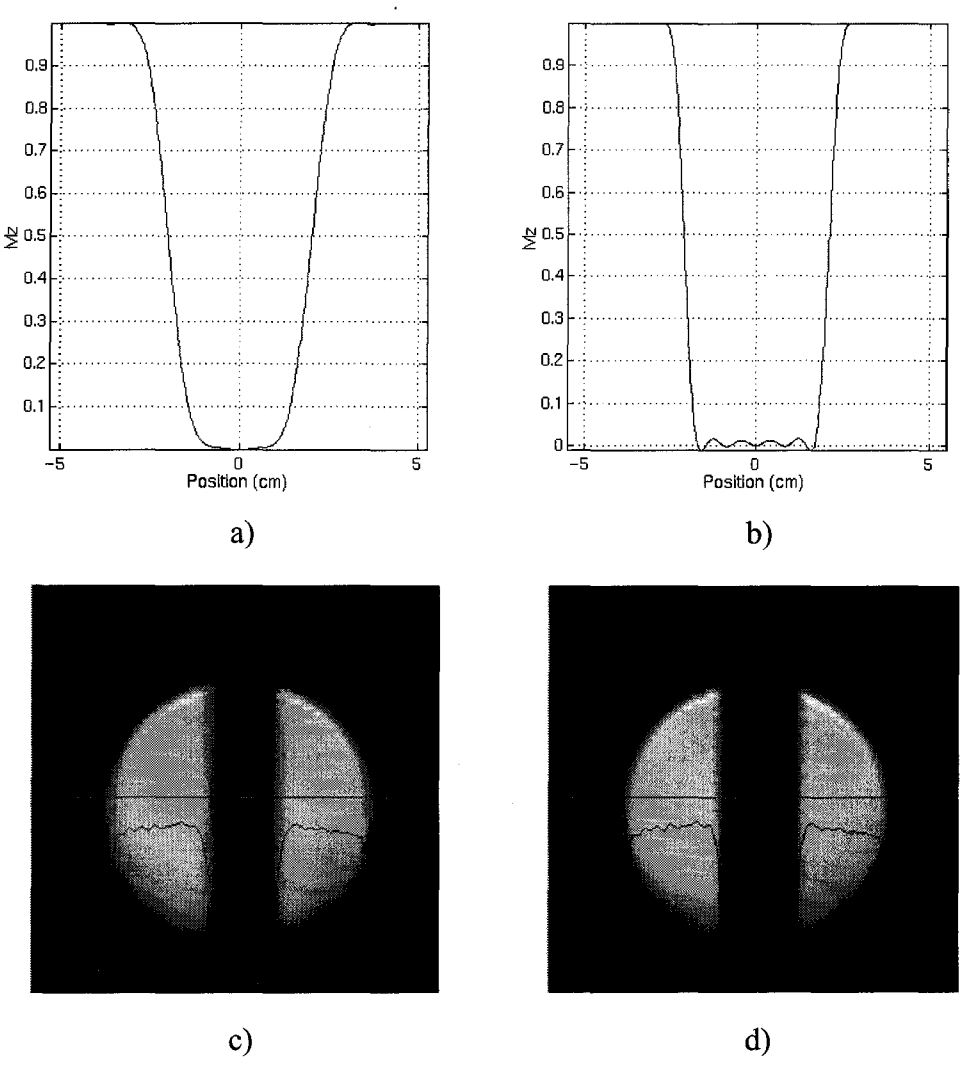

Figure 4.10: Simulator and flood phantom profiles for a standard Siemens presaturation pulse [a) and c)] and the optimized presaturation pulse chosen for use in PICORE sequences [b) and d)]. Profiles are shown for a slice thickness of 48 mm and a pulse time of 2.56 ms.

The optimized pulse depicted in Figure 4.10 b and d has much better profile characteristics compared to the standard Siemens presaturation pulse in Figure 4.10 a and c. This improved profile was found to efficiently minimize the interaction between the inversion tag and the static tissue in the imaging region thus improving the detection of CBF changes using the PICORE technique.

Selection of the Q2TIPS periodic saturation pulse was based on slice profile characteristics for a 20 mm slice. This thickness, as well as the pulse duration of 3.2 ms,

was chosen to comply with the parameters of the original Q2TIPS implementation [37]. Since the size of the tagging region and the Q2TIPS saturation region remains constant regardless of image slice thickness, separation and number, it was unnecessary to ensure good slice profile characteristics at other saturation thicknesses. The final Q2TIPS saturation pulse chosen was a 15-lobe least-squares filtered sinc pulse designed using RF Tools. The simulation and phantom profiles for this pulse is shown in Figure 4.11 along with the original Q2TIPS saturation pulse used by Luh *et al.*.

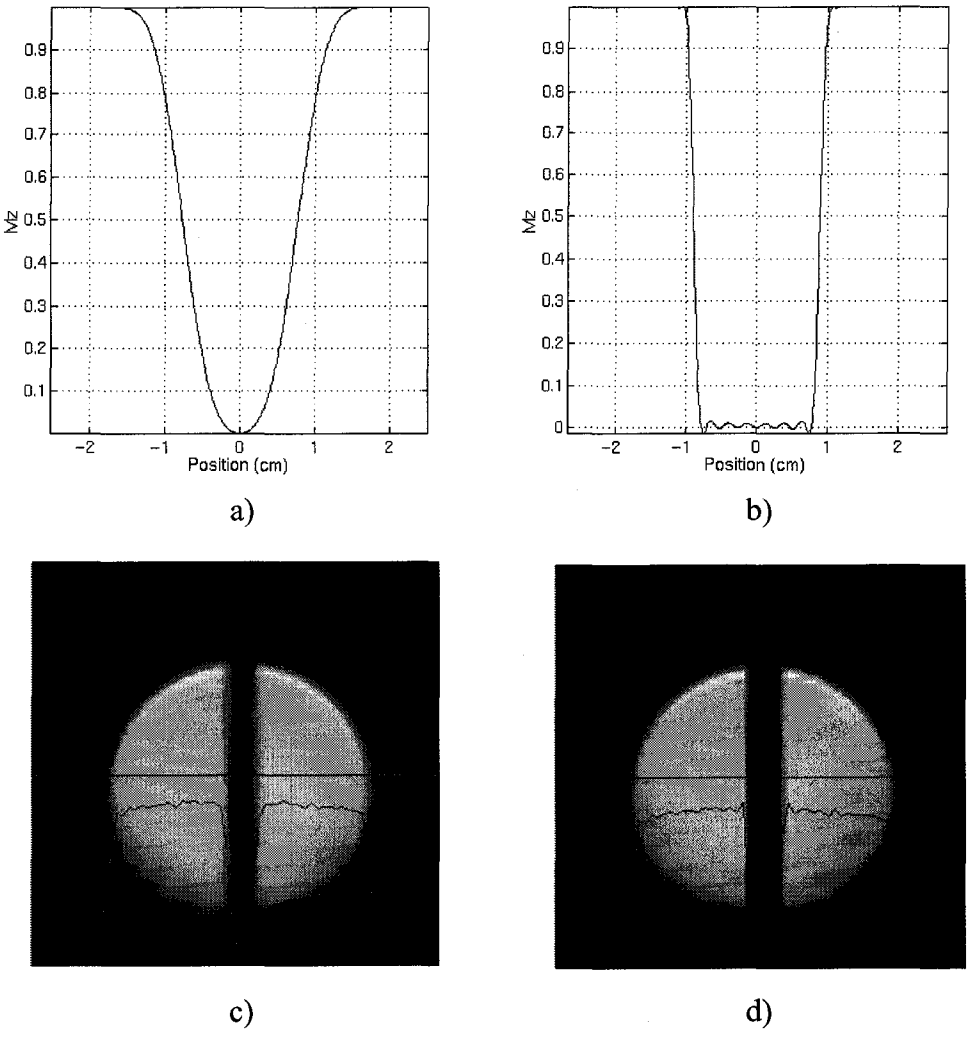

Figure 4.11: Simulator and flood phantom profiles for the pulse used in the original implementation of Q2TIPS [a) and c)] and the optimized Q2TIPS saturation pulse [b) and d)]. Profiles are shown for a slice thickness of 20 mm and a pulse time of 3.2 ms.

The saturation profile of the 15-lobe sinc pulse depicted in Figure 4.11 b and d is much better then the profile of the 3-lobe pulse used in the original implementation of Q2TIPS shown in Figure 4.11 a and c. This improved profile further minimized the mismatch between the distal edge of the saturation and inversion pulse profiles in Q2TIPS thus increasing the accuracy of the quantitative CBF measurements acquired using this technique.

Chapter 5

Experimental Validation

5.1 Presentation of Visual Stimulus

Although quantitative ASL techniques are capable of providing measurements of resting state cerebral perfusion, the main purpose of this ASL implementation in our lab is for studying functional brain activations with specific goals aimed at comparing ASL results with those obtained using BOLD imaging techniques [16, 17]. As a result, experimental validations of the final ASL sequences were performed using robust visual stimuli to activate the visual cortex. Visual stimuli were chosen due to the relatively large signal response typical from this type of stimuli as well as the known location and functional organization of the visual areas [42]. Presentation of the visual stimuli was accomplished using an LCD video projector and screen setup in conjunction with a mirror mounted on the RF head coil. A schematic of the stimulus presentation apparatus is displayed in Figure 5.1.

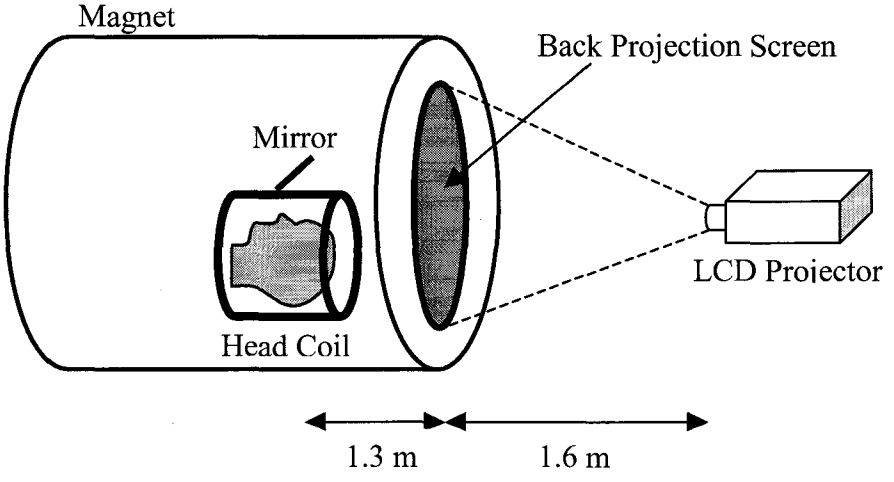

Figure 5.1: Visual stimulus presentation apparatus and setup. An LCD projector is used to project images onto a back projection screen mounted on the end of the magnet bore. The subject views the images through a specially designed mirror which attaches to the RF head coil.

The visual stimulus used for activation throughout this thesis consisted of an alternating yellow and blue radial checkerboard pattern with 100% luminance contrast.

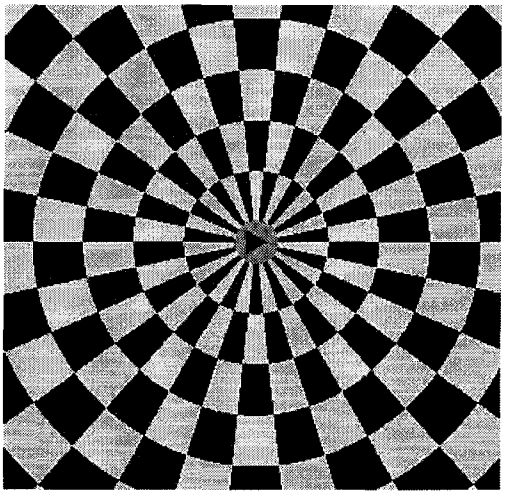

Figure 5.2: Alternating radial checkerboard pattern used for visual stimulus. During stimulus the yellow/blue colour scheme was set to alternate at 8 Hz. A fixation arrowhead in the center of the pattern randomly switched direction for subject feedback.

In order to ensure subject fixation on the pattern, a small arrowhead was placed in the center of the checkerboard. This arrowhead was set to randomly switch directions from left to right and subjects were asked to report its orientation by pressing the corresponding button on an MRI-compatible mouse. Generation of the stimulus as well as recording of the subject feedback was accomplished using OpenGL-based software [43] on a Silicon Graphics O_2 computer (Silicon Graphics Inc., California, USA).

5.2 Final Sequence Details

The implementation of the PICORE/Q2TIPS arterial spin labelling technique was performed on a Siemens 1.5 Tesla Magnetom Vision system (Siemens Medical Systems, Erlangen, Germany) using a quadrature birdcage transmit/receive RF head coil. A standard EPI acquisition base sequence was chosen as a platform on which to assemble the final ASL sequence. This base sequence consisted of a gradient echo, single-shot EPI acquisition with a 90° flip angle RF excitation, a receiver bandwidth of 125 kHz, a readout time of 512 μs, a 64×64 matrix size, a TE = 26.76 ms and a minimum TR = 75.83

ms (per slice). This EPI sequence also included a fat suppression component employing spectral presaturation pulses. The final hyperbolic secant inversion pulse, presaturation pulse and Q2TIPS saturation pulse discussed in the previous chapter were added to this base sequence appropriately to create a quantitative Q2TIPS sequence as well as an interleaved Q2TIPS/BOLD sequence. Both of these sequences included oscilloscope trigger pulses for synchronization with functional stimuli as well as user adjustable inversion times, repetition times, slice number (up to a maximum of 16), slice thickness and slice separation. The interleaved Q2TIPS/BOLD sequence consisted of four image acquisitions per run (Q2TIPS control → BOLD → Q2TIPS tag → BOLD). For BOLD acquisitions an echo time of 50 ms was used with a TR = 1.5 s. All other EPI acquisition parameters were identical for the BOLD and Q2TIPS measurements.

5.3 Sequence Stability

Testing of the final multi-slice quantitative PICORE/Q2TIPS sequence began with a series of tests-retests to ensure quantitative regional CBF measurements were stable over time. These stability tests were conducted through repeated measurement of a single resting subject over a reasonable time-span.

MATERIALS AND METHODS

Stability of the PICORE/Q2TIPS sequence was tested over a course of 3 weeks. Using the Q2TIPS sequence, quantitative regional CBF images were acquired on 4 separate occasions using a contiguous 9-slice technique with a slice thicknesses of 8 mm, a TR = 3 s, and a field-of-view (FOV) of 256 mm. Q2TIPS specific parameters included TI_1 = 700 ms, TI_2 = 1400 ms and TI_{1s} = 1200 ms with a total of 21 periodic Q2TIPS saturation pulses. In order to produce high-signal-to-noise ratio subtraction images, 100 averages were collected requiring a scanning time of 10 minutes.

The acquired images were processed using a routine written in the Perl scripting language (Perl Version 5.001). This routine first converted the images from the raw NEMA data format of the MR unit to MINC format (a format created at the MNI to facilitate easy post-processing of images) [44]. Once in MINC format, the images were

separated into tag and control images and image subtraction was performed to produce ASL weighted difference images.

Using Equation 3.6 to arrive at absolute perfusion values requires knowledge of both the signal from fully T_1 relaxed blood (M_{oB}) as well as T_{1B}. T_{1B} was estimated at 1300 ms for all measurements. M_{oB} was determined in the same manner used by Wong *et al.* in the original implementation of QUIPSS and QUIPSS II [27]. This method makes use of the relationship:

$$M_{oB} = RM_{oWM} e^{\left(\frac{1}{T_{2WM}} - \frac{1}{T_{2B}}\right)TE}, \qquad (5.1)$$

where M_{oWM} is the fully T_1 relaxed signal from white matter, R is the measured ratio of proton density of blood in the sagittal sinus to that of white matter, and T_{2WM} and T_{2B} are assumed to be 80 ms and 200 ms respectively. The value of R was measured using a proton density weighted, high-resolution, gradient-echo conventional image (TE = 5ms, TR = 1000 ms, $\alpha = 10°$) while M_{oWM} was measured from a single-shot EPI image with a TR = ∞.

Analysis of the images was carried out over a large region-of-interest encompassing the visual cortex. The subject chosen for these stability tests had previously undergone activation analysis using a visual stimulus in conjunction with a well established BOLD imaging technique. As a result, statistical maps defining a large region-of-interest encompassing the visual region of the brain already existed. The means by which these maps were created is described in the next section covering functional testing of the Q2TIPS sequence. The activation ROI was individually registered to each 9-slice Q2TIPS acquisition set using high-resolution anatomical images that indicated the transformation of the brain position between scans. The average CBF value over this region of interest was calculated for each scan and the stability of the results determined using statistical analysis.

RESULTS AND DISCUSSION

Difference images from a typical 9-slice acquisition are shown in Figure 5.3 along with the corresponding T_1-weighted anatomical images for each slice.

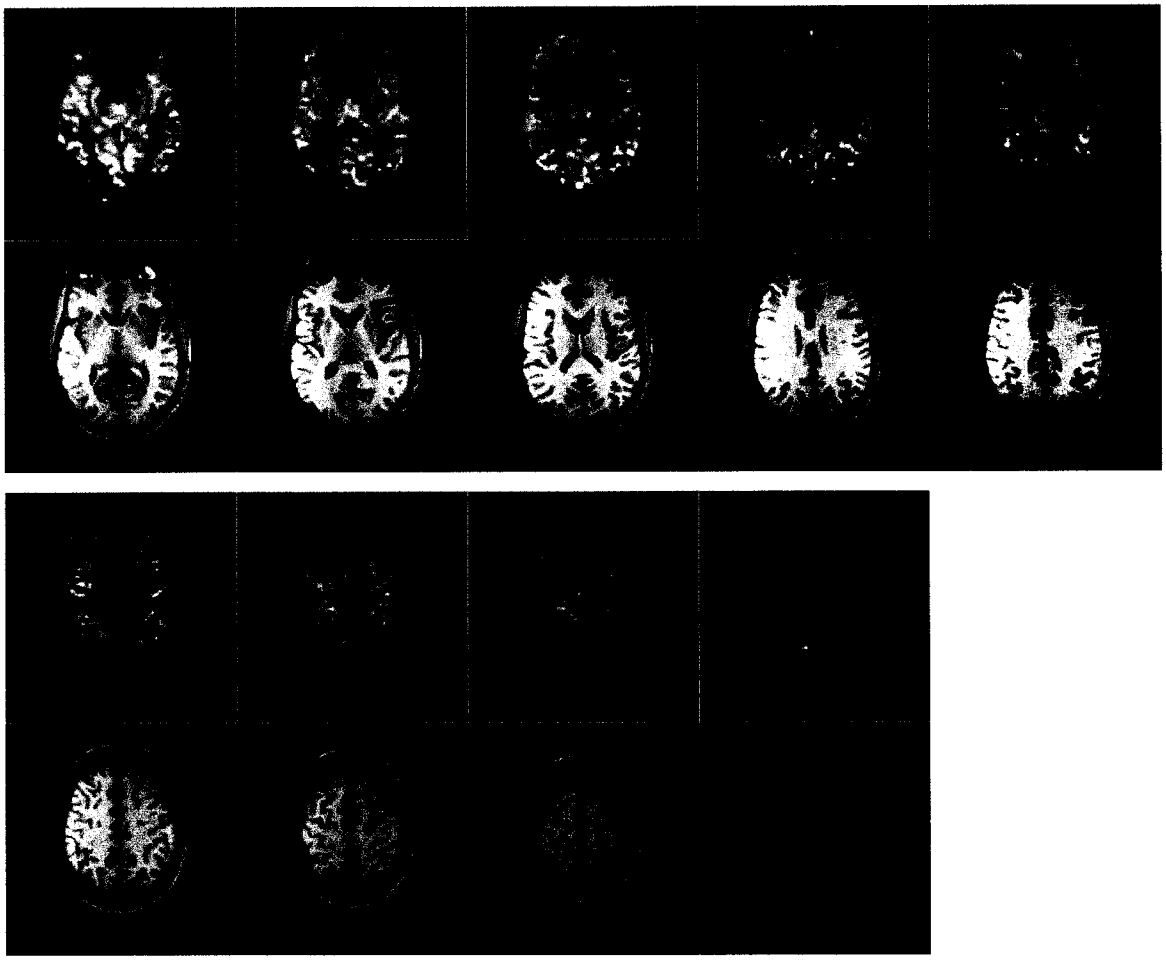

Figure 5.3: Q2TIPS difference images of subject at rest acquired with a 9-slice contiguous acquisition. Anatomical T_1-weighted images of the corresponding slices are shown below.

As expected, initial inspection of the Q2TIPS images in Figure 5.3 indicate increased cerebral blood flow in the gray matter compared to white matter. Also evident is the decrease in the ASL signal from proximal to distal slices. This decrease is a result of decay of the tag due to longitudinal relaxation. Since the images are acquired in ascending order, distal slices are acquired last thus showing more signal loss.

The BOLD-based, visual activation regions-of-interest used during analysis of the stability of the sequence are shown in Figure 5.4.

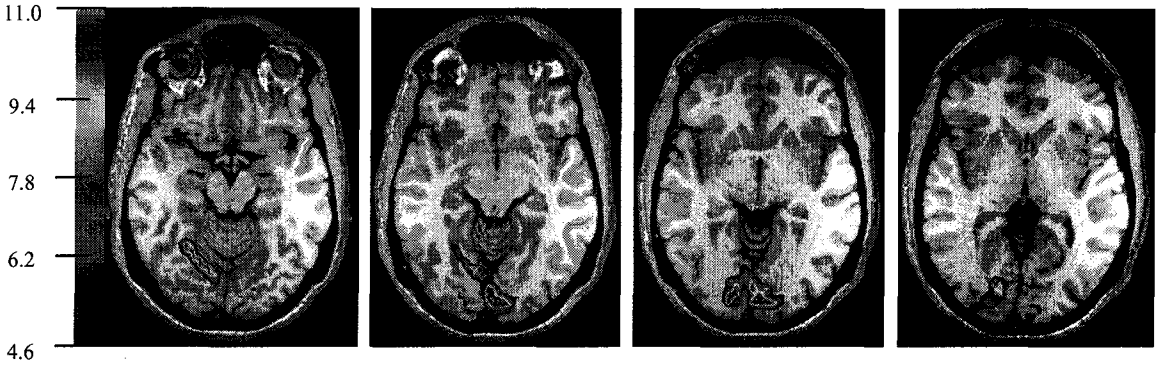

Figure 5.4: Large ROI encompassing the visual cortex as acquired previously using a robust multi-slice BOLD imaging technique. ROIs have been superimposed on grayscale T_1-weighted anatomical images of the corresponding slice.

As expected, the ROIs cover a large portion of the occipital lobe that corresponds to the known localization of the visual cortex. Averages of the regional CBF were calculated over this ROI for all three 9-slice Q2TIPS acquisitions. These averages are displayed in Table 5.1.

Scan Number	Average CBF Over ROI (mL/100 g tissue/min)
1	50.5 ± 19.6
2	44.9 ± 20.3
3	46.3 ± 19.7
4	48.5 ± 18.4

Table 5.1: Regional CBF averages from visual cortex ROI from a single subject over a time-span of 3 weeks. Errors represent the standard deviation of the CBF over the activated voxels.

The errors displayed in Table 5.1 were calculated by taking the standard deviation of the CBF values over the activated voxels. From visual inspection of these results it is obvious that there is not a great deal of variation in the CBF values over time. Statistically the standard deviation over the scans is 2.46 mL/100 g tissue/min indicating that the data acquired over the 3 week period was probably not significantly different.

5.4 Functional Quantitative ASL Measurements

The next step in validating the implemented Q2TIPS sequence was to test its own applicability to detecting functional brain activation. In these tests, a block-design visual stimulus was displayed to subjects during measurement using the Q2TIPS sequence.

MATERIALS AND METHODS

In order to induce brain activation, the radial checkerboard visual stimulus described previously was employed. This visual stimulus was interleaved with a control (baseline) presentation consisting of a uniform gray background to form a 5 stage block-design paradigm (control → stimulus → control → stimulus → control) with a stage duration of 2 minutes. An illustration of this paradigm is shown in Figure 5.5.

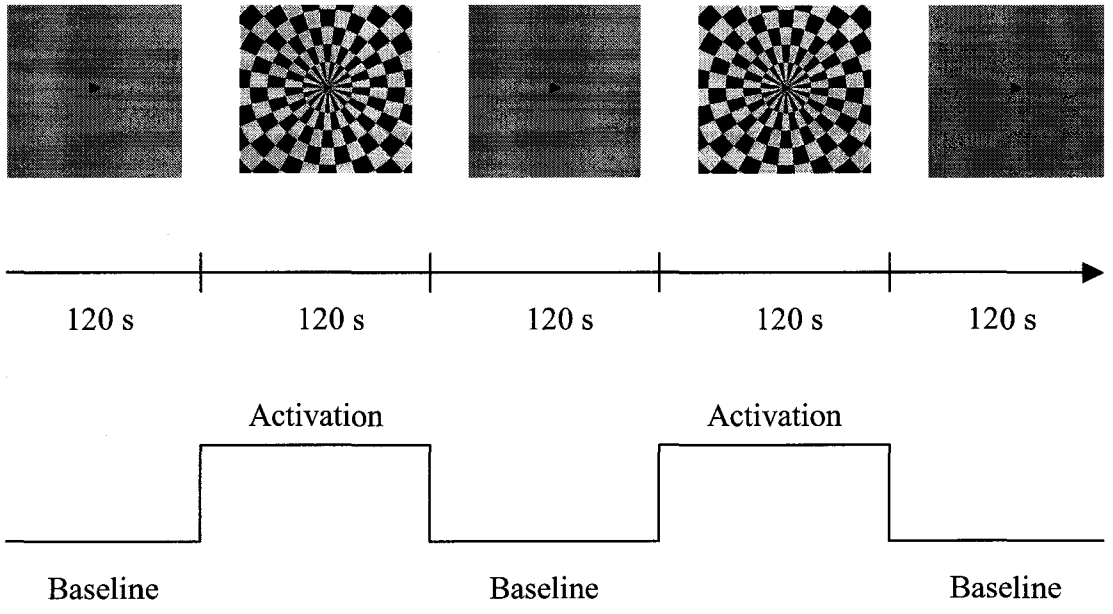

Figure 5.5: Five-stage visual stimulus paradigm used to test applicability of sequence to detect function brain activation. Each stage of paradigm has a duration of 2 minutes for a total duration of 10 minutes.

For a total of 8 subjects, quantitative regional CBF images were acquired using a contiguous 5-slice technique with a slice thicknesses of 8 mm, a field-of-view of 256 mm, a matrix size of 64 × 64, and a TR = 2.5 s. Using this TR, a total of 120 difference images were acquired over the entire length of the paradigm (24 images per stage).

Slices were oriented obliquely, parallel to the calcarine fissure, in the occipital cortex so as to maximize coverage of the visual area of the brain. Image processing and calculation of quantitative regional CBF images were carried out as described in Section 5.3 above.

In order to determine regions of functional brain activation the quantitative time series was analyzed using an in-house, MATLAB based, parametric fMRI statistical analysis program called fMRIstat [45]. This program was employed to correlate the visual stimulus presented to the subjects with changes in the regional CBF to produce statistical t-maps.

RESULTS AND DISCUSSION

Quantitative regional CBF images from a 5-slice contiguous acquisition are displayed in Figure 5.6.

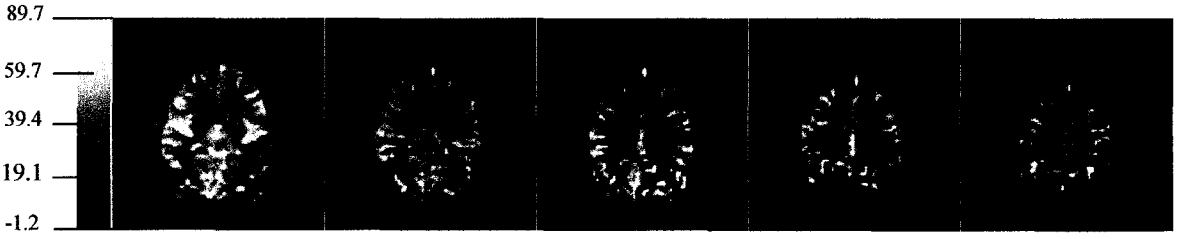

Figure 5.6: Quantitative regional CBF maps from a 5-slice acquisition through the occipital lobe. The grayscale bar on the left indicates regional CBF values in units of mL per 100 g tissue per minute.

Figure 5.7 shows examples of typical activation regions detected through parametric statistical analysis using fMRIstat.

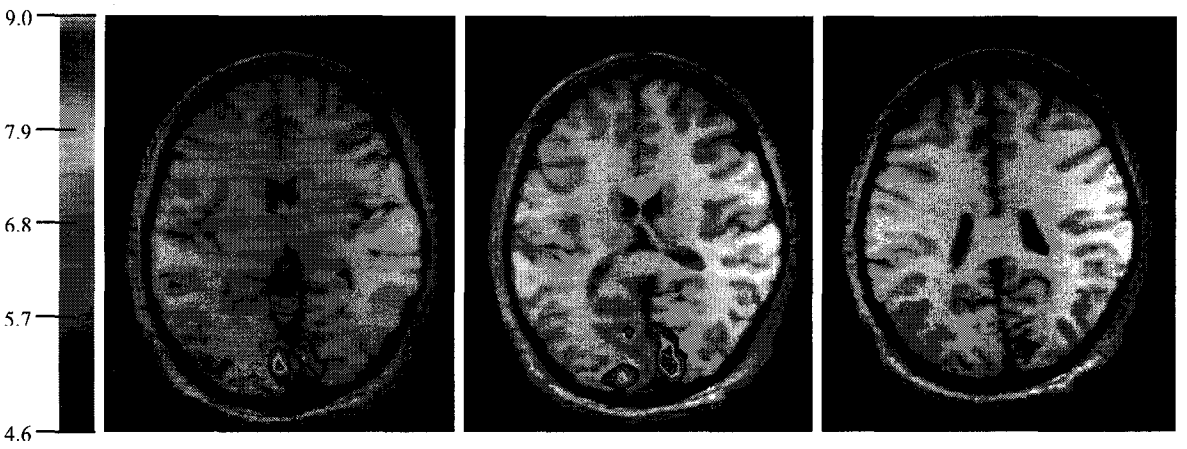

Figure 5.7: Parametric statistical t-maps produced by time course analysis using fMRIstat superimposed on grayscale T_1-weighted anatomical images of the corresponding slice. The colour bar indicates t-values. Here a t-value ≥ 4.61 corresponds to a statistical significance of $p \leq 0.05$.

In order to spatially localize the brain activations, the t-maps in Figure 5.7 have been superimposed on registered anatomical images. These images show brain activations in the occipital region of the first three imaging slices. The time courses for all of these regions is shown in Figure 5.8.

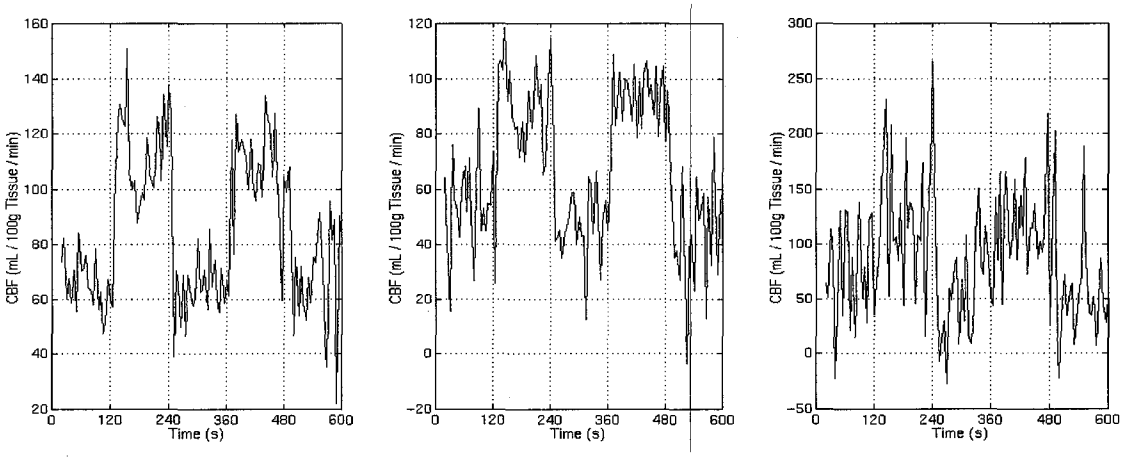

Figure 5.8: Time-courses for activated voxels (t-value $\geq$ 4.61) from Figure 5.7. Activations between 120 s $\rightarrow$ 240 s and 360 s $\rightarrow$ 480 s are apparent. The first three data points were excluded from the analysis since they don't represent steady-state magnetization images.

In Figure 5.8, activations are apparent in all three slices for the time intervals where the radial checkerboard was presented. Although the first two slices show excellent activation profiles the third slice was found to be quite noisy. This noise can be predicted from examination of the t-maps in Figure 5.7. The t-values of the significant voxels in this slice are noticeably lower then the t-values in the other two slices. Closer examination indicates these voxels were in fact on the edge of being statistically significant at the $p = 0.05$ level. In order to avoid such data from confounding results, the t-threshold used for the remainder of the analysis was increased to a value of 5 which corresponds to a statistical significance of $p = 0.01$. Averaging of the regional CBF values from activated voxels over all slices for both baseline and activated regions yields a baseline rCBF = 48.8 mL/g tissue/minute and an activated rCBF = 85.2 mL/g tissue/minute. Identical analyses were conducted on all 8 subjects. The data from these analyses is displayed in Table 5.2.

Subject	Resting State rCBF (mL/100 g tissue/min)	Activation State rCBF (mL/100 g tissue/min)	Percent Increase (%)
1	48.8 ± 20.9	85.2 ± 25.1	74.6
2	87.7 ± 16.6	122.6 ± 21.1	39.8
3	56.4 ± 21.8	82.2 ± 24.2	45.7
4	72.8 ± 20.6	108.5 ± 19.9	49.0
5	58.7 ± 23.7	80.8 ± 24.7	37.6
6	50.9 ± 18.4	75.9 ± 18.2	49.1
7	65.1 ± 19.9	91.3 ± 23.3	40.2
8	61.6 ± 14.3	90.1 ± 18.0	46.3
Average	62.7 ± 12.6	91.9 ± 15.8	47.8 ± 11.7

Table 5.2: Regional CBF values for the visual cortex of all 8 subjects. Data consists of averaged rCBF values from voxels with t-values ≥ 5. Errors displayed for individual subjects represent the standard deviation over all time frames while the error in the average represents the standard deviation over all subjects.

Errors in the data from each subject were calculated by taking the standard deviation over all time frames from the resting and activation state intervals. Errors in the average were calculated by taking the standard deviation over the values from each subject.

Upon examination of the results in Table 5.2 it is obvious that cerebral blood flow values vary significantly from subject to subject for both resting states and activation states. This finding may explain the presence of large inconsistencies in CBF values found in the literature. For resting subjects, literature CBF values range from 30 mL/100 g tissue/min [27] to up to 91 mL/100 g tissue/min [30] for a variety of MR measurement techniques including CASL, PASL, and dynamic susceptibility contrast (DSC) imaging [46-50]. These inconsistencies are also present when other imaging modalities are used for CBF measurement. Xe computed tomography techniques have measured CBF values as high as 85 mL/100 g tissue/min [51] while quantitative PET studies usually measure values from 50 to 67 mL/100 g tissue/min [48, 52, 53, 54]. Considering the variations in CBF detected using these various techniques, the average calculated in Table 5.2 is in good agreement for CBF for resting subjects. The average CBF calculated in the visual cortex during the activation stages was found to be low compared to similar data measured by Yang *et al.* using a sensorimotor cortex stimulation [33]. Using self-paced sequential thumb-to-digit oppositions with both hands, this study detected average CBF values of 66.8 mL/100 g tissue/min for rest and 120.6 mL/100 g tissue/min for activation. In order to compare the results of our study with those acquired using an identical activation stimulus the percent increase in CBF was calculated in Table 5.2. The percent increase results calculated here agree very well with a similar study carried out in our lab using a single-slice qualitative FAIR acquisition [17]. In that study an identical visual stimulus was found to produce CBF percent increases of 48 ± 5 % whereas we observed percent increases of 47.8 ± 11.7 % in the current study.

In order to visualize the activation data over all subjects, a mean time-course was created by averaging the CBF values from activated voxels ($t \geq 5$) over all subjects at each time frame of the acquisition. The resultant time-course is displayed in Figure 5.9.

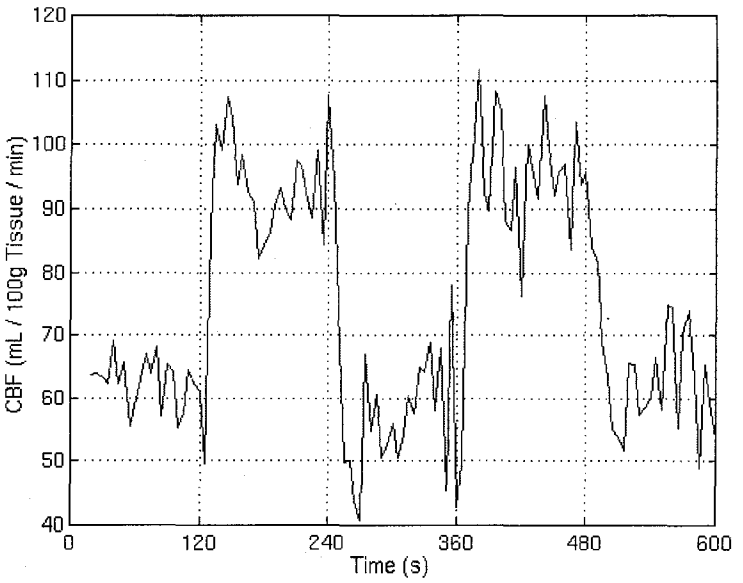

Figure 5.9: Average time-course for all 8 subjects. This time-course was created by averaging all statistically significant ($t \geq 5$) subject data for each time point.

5.5 Interleaved Q2TIPS/BOLD Imaging

The final validation of quantitative multi-slice ASL implementation involved testing the interleaved Q2TIPS/BOLD sequence. This validation involved carrying out a brief study comparing the signal changes in, and localization of, brain activations detected using the BOLD signal with those detected using regional CBF from the Q2TIPS signal.

MATERIALS AND METHODS

Validation of the Q2TIPS/BOLD sequence made use of the same block-design stimulus described in Section 5.4. For 8 subjects, Q2TIPS and BOLD images were acquired using a contiguous 5-slice technique with a slice thicknesses of 8 mm and an FOV of 256 mm. Repetition times were set to TR = 2.5 s for Q2TIPS acquisitions and TR = 1.5 s for BOLD acquisitions. These settings resulted in the acquisition of 2 BOLD images and 1 Q2TIPS subtraction image (1 tag and 1 control image) every 8 seconds. BOLD images from every 8 second period were averaged together for a total of 75 final BOLD and Q2TIPS subtraction images over the length of the paradigm (15 image sets per stage). Slices were again oriented obliquely over the calcarine fissure in the occipital cortex.

BOLD and perfusion time courses were analyzed separately for activation regions using fMRIstat.

RESULTS AND DISCUSSION

Examples of typical t-maps from a single subject acquired for both BOLD and Q2TIPS acquisitions using the interleaved sequence are shown in Figure 5.10.

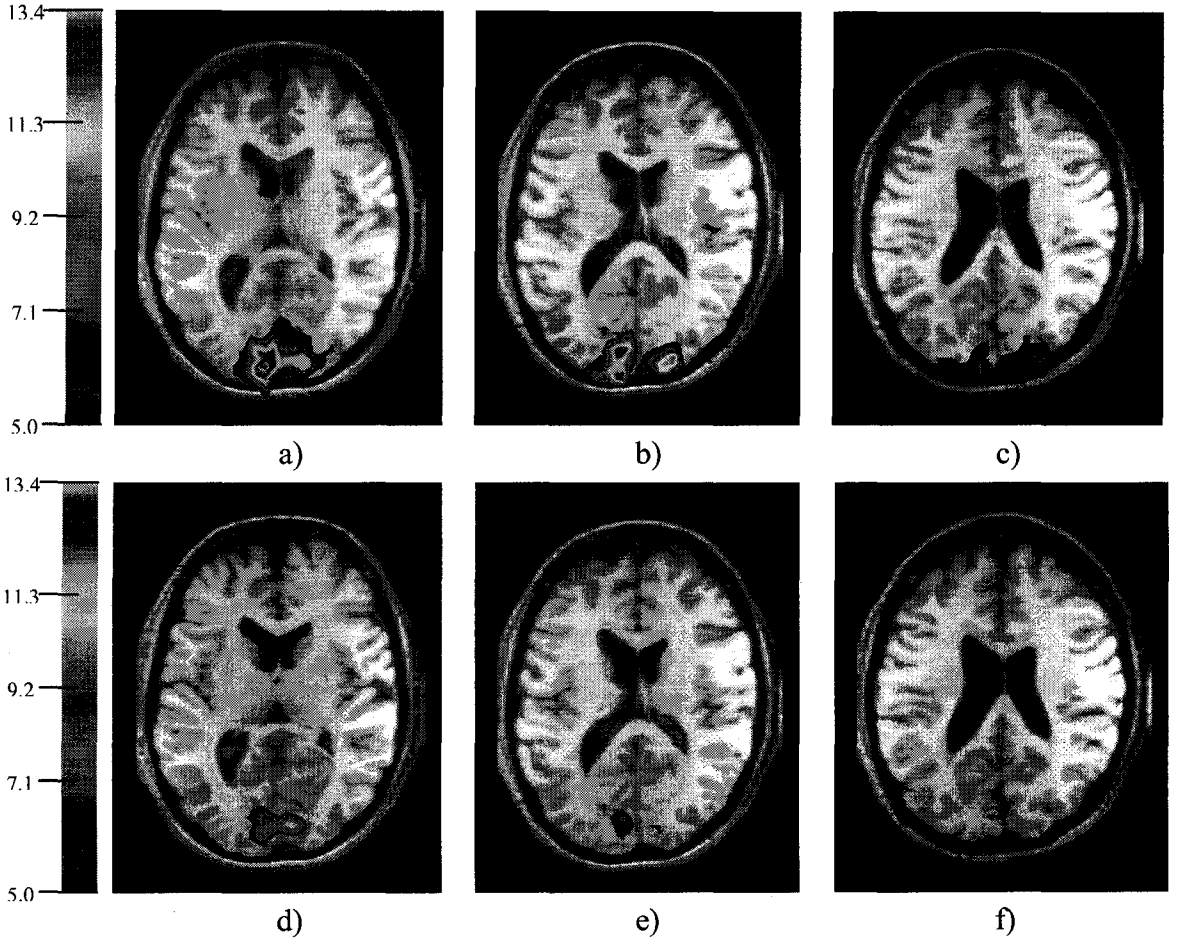

Figure 5.10: Statistical t-maps for BOLD acquisitions [a) to c)] and Q2TIPS acquisitions [d) to f)] from interleaved sequence. Images a) and d) correspond to the same slice as do images b) and e) and images c) and d). For all images $t \geq 5$.

Images a) through c) were created by running fMRIstat on the BOLD images acquired from one subject. These images show large regions of interest in the occipital lope

corresponding to increases in the BOLD signal with activation. Images d) through f) were created using the Q2TIPS images for the same slices.

The most obvious difference between the statistical t-maps from both techniques is the size of the significant regions. Although for the first two slices the locations of the activations are very similar, the activation regions detected using the BOLD technique are noticeably larger then those detected using Q2TIPS. While the BOLD region spans 3 slices and encompasses a total of 178 voxels, the Q2TIPS region only spans 2 slices and is made up of a total of 35 voxels. Additionally, the t-values in the activation maps created using the BOLD data set are noticeably higher then those in the maps created using the Q2TIPS data.

The averaged time-courses for these regions are shown in Figure 5.11.

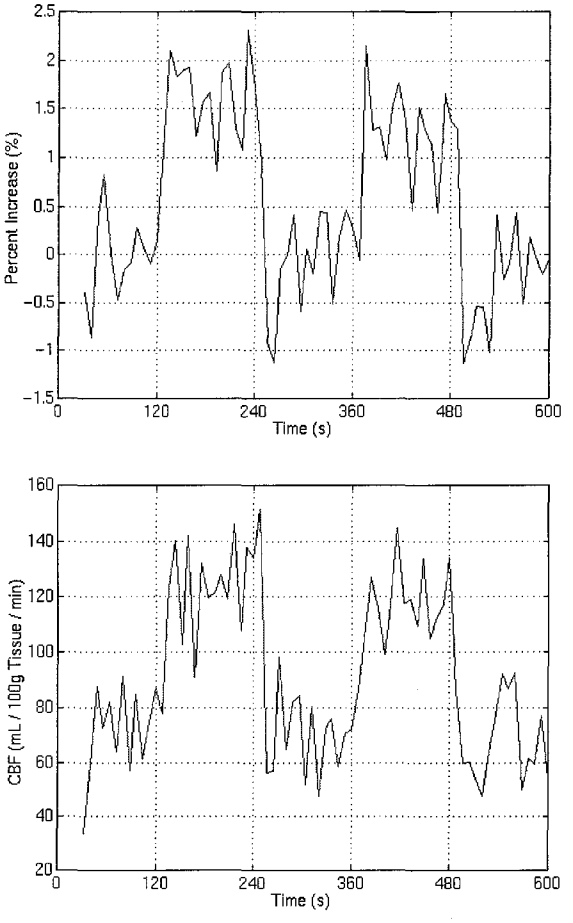

Figure 5.11: Averaged time-courses for activated voxels (t-value ≥ 5) from Figure 5.10. The first plot represents the averaged time-course for the BOLD acquisitions while the second plot represents the averaged time-course for the Q2TIPS acquisitions.

Averaging of both the BOLD percent increase and regional CBF values from activated voxels for both baseline and activated regions yields a baseline rCBF = 75.9 mL/g tissue/minute, an activated rCBF = 120.4 mL/g tissue/minute and an activated BOLD signal increase of 1.6 %. Identical analyses were conducted on all 8 subjects. The data from these analyses is displayed in Table 5.3.

Subject	Rest CBF (mL/100 g/min)	Activation CBF (mL/100 g/min)	# Voxels (Q2TIPS)	BOLD Signal Percent Increase	# Voxels (BOLD)
1	75.9 ± 22.6	120.4 ± 30.7	41	1.6 ± 0.6	176
2	37.0 ± 21.4	62.2 ± 23.3	6	2.0 ± 0.7	37
3	68.5 ± 25.4	101.9 ± 27.6	24	2.1 ± 0.4	81
4	52.5 ± 29.0	95.1 ± 31.3	35	1.6 ± 0.4	178
5	71.7 ± 28.4	107.5 ± 29.7	28	2.3 ± 0.5	118
6	43.7 ± 29.9	76.9 ± 30.8	21	1.9 ± 0.6	83
7	57.6 ± 22.4	91.3 ± 29.2	28	2.9 ± 0.5	87
8	46.8 ± 20.8	79.1 ± 23.1	30	1.4 ± 0.3	137
Avg.	56.7 ± 14.2	91.8 ± 18.6	26 ± 10	2.0 ± 0.5	112 ± 49

Table 5.3: Regional CBF values and BOLD signal percent increase for the visual cortex of all 8 subjects. Data corresponds to voxels with t-values ≥ 5. Errors displayed for individual subjects represent the standard deviation over all time frames while the errors in the average represents the standard deviation over all subjects.

Once again, errors in the data from each subject were calculated by taking the standard deviation over all time frames from the resting and activation state intervals while errors in the average were calculated by taking the standard deviation over the values from each subject.

As expected, values for the rest and activation CBF over the regions-of-interest are very similar to those found using Q2TIPS alone. One noticeable difference between these values and those in the previous section, however, is in the standard deviations over all time frames for each subject. In the Q2TIPS-only acquisition data, the average of these standard deviations over all subjects was 19.5 for resting stages and 21.8 for activation stages. The same values for the interleaved acquisition data in Table 5.3 are 25.0 for resting stages and 28.2 for activation stages. This increased error in the data acquired using the interleaved sequence is most likely a result of decreased time-resolution inherent from this sequence. Subtracted images in the Q2TIPS-only method

are separated by 2.5 s while the same subtracted images in the interleaved method are separated by 4 s. While the difference in time separations is small, it certainly causes the interleaved acquisitions to be more susceptible to motion artifacts which can add appreciable noise to the subtraction images.

The BOLD signal percent increase of 2.0 ± 0.5 % calculated over the entire set of subjects was found to be in good agreement with previous BOLD experiments conducted in our lab using the same visual stimulus pattern [13, 16, 17, 55]. Similar results have also been reported by other groups. Gati *et al.* reported an ~ 2 % average BOLD change in cortical gray matter during visual stimulation [56] while Zhu *et al.* found an percent increase of 1.7 % using a similar setup [57].

Larger activation regions from BOLD data compared to those found using perfusion data have been reported in several previous studies comparing BOLD and perfusion imaging [46, 57, 58]. A significantly larger number of activated voxels for BOLD data sets was reported by Kim *et al.* in a study comparing BOLD and FAIR measurements [34]. In this study, the average number of voxels from BOLD data sets was roughly double that from FAIR data sets. The increased size of the activated region in BOLD data sets is believed to be due to the large macrovascular contribution in BOLD images and is one of reasons why many researchers hold that signal changes detected by BOLD imaging may be remote to the activated cortex. On the other hand, perfusion measurements are localized to microvasculature (microscopic capillaries) and are therefore likely to represent the sites of neuronal activity better then BOLD activation maps. Although this explanation for the difference in the size of the activated regions may be true, another possible explanation may be the difference in signal-to-noise ratio (SNR) between the BOLD and perfusion data sets. As observed in the time-courses in Figure 5.11, the perfusion data from the Q2TIPS technique was found to have a lower SNR compared to the BOLD data. This was found to be the case with all subjects and is an expected result due to the much lower signal intensity measured in perfusion imaging as well as the fact that the image subtraction in the perfusion technique is very sensitive to subject motion. Lower SNR in the perfusion data has the potential of decreasing the activation size when parametric statistical analyses are performed. In this case the increased relative noise would drown out the signal in regions where the signal is lower.

As this occurs at the edges of the activated region, the apparent activation size should be smaller. In order to determine which of these explanations is more dominant would require an increase in the SNR in the perfusion data set.

Once again an average time-course was created by averaging the CBF values from activated voxels ($t \geq 5$) over all subjects at each time frame of the acquisition. The time-courses for both the BOLD percent increase and the CBF over the total group of subjects is displayed in Figure 5.12.

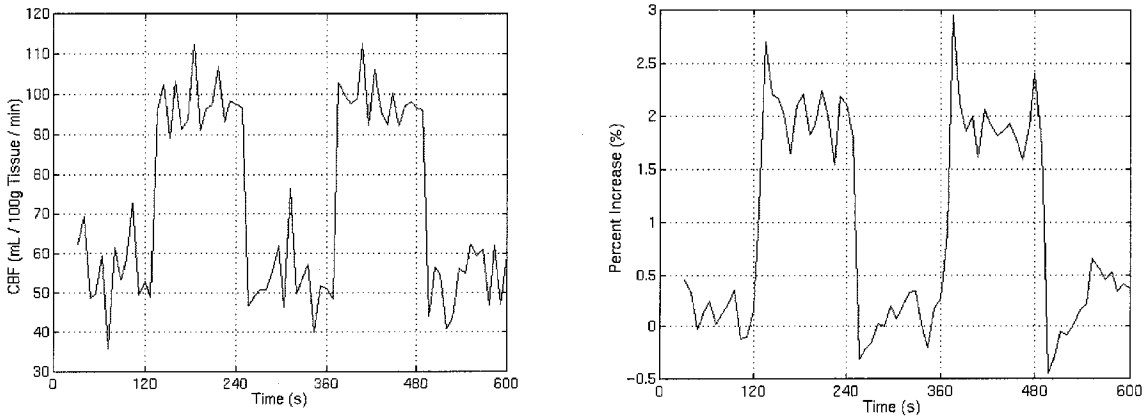

a) b)

Figure 5.12: Average time-courses for a) CBF values from Q2TIPS acquisition and b) the BOLD percent increase over all 8 subjects. Time-courses were created by averaging all statistically significant ($t \geq 5$) subject data for each time point.

Chapter 6

Conclusions and Further Work

6.1 Conclusions

The main focus of this thesis was the development, implementation, and optimization of a quantitative multi-slice perfusion imaging technique to replace the qualitative single-slice perfusion technique which was previously in use in our lab. Following a thorough literature review on perfusion imaging methods, it was decided that a multi-slice PICORE/Q2TIPS sequence be utilized. Development of this pulse sequence entailed several steps including the design of an appropriate inversion pulse for arterial labeling, spatial offset of this pulse as required by the base PICORE arterial spin labeling method, and development of both presaturation and Q2TIPS saturation pulses for use in the final quantitative sequence. Once completed, these individual components were incorporated into a multi-slice gradient-echo EPI acquisition with a 64 × 64 matrix size and a minimum TR = 75.83 ms per slice. The final Q2TIPS sequence was thoroughly tested with respect to both measurement stability and applicability to fMRI experiments. Preliminary test results indicate that this sequence provides a robust technique through which absolute CBF measurements can be acquired. Following experimental validation of the sequence output a BOLD-interleaved version of the sequence was implemented.

The new Q2TIPS perfusion sequence introduces three main improvements over the previous perfusion imaging method: increased spatial coverage, increased time resolution, and the acquisition of quantitative regional CBF values. Use of the previous single-slice perfusion technique required careful positioning of the slice in order to cover as much of the desired activation focus as possible. The Q2TIPS sequence introduced is capable of imaging up to 9 contiguous slices with a slice thickness of 8 mm thus enabling imaging of the entire cerebrum. This increase in the spatial coverage is sure to make positioning of slices much easier even when acquiring data from activation foci which are

not easily identified. The time resolution of the new Q2TIPS method is approximately 8 seconds for interleaved perfusion and BOLD measurements. This is an improvement over the previous technique which required 12 seconds for one set of TAG-BOLD-CONTROL-BOLD images. The final major improvement of the new sequence over the previous technique is the acquisition of quantitative regional cerebral blood flow values compared to the acquisition of qualitative CBF percent increase values. These absolute values of CBF allow not only for direct validation with quantitative PET CBF measurement methods but also allow for CBF measurement in resting state subjects without any activation stimulus thus opening the door to many possible medical applications including stroke evaluation and localization of epileptic foci.

6.2 Further Work

Further work on the sequence implemented in this thesis should be aimed at directly validating the CBF values acquired. A quantitative comparison with PET should be performed on the same subjects for the same visual stimulus in order to further establish the accuracy of this method.

Work should also be conducted in order to expand the utility of this sequence for use in B_0 inhomogeneous regions of the brain where BOLD is not useful. This endeavor can be accomplished by replacing the current EPI readout with a fast spin echo (FSE) readout. Once completed, this would provide a useful fMRI method for imaging regions such as the orbital frontal cortex.

Finally, an investigation should be carried out to explore the possibilities of simultaneous BOLD/Q2TIPS imaging. These techniques have been attempted by other groups and would essentially increase the time resolution of the interleaved BOLD/Q2TIPS technique by at least 3 seconds. This increase in time resolution would allow for the acquisition of other interleaved data sets with perfusion such as cerebral blood volume measurements. As mentioned previously in this thesis, investigation of the interplay between CBF, CBV, and the BOLD signal is a subject of interest in our lab. The quantitative multi-slice perfusion sequence developed during this project will eventually be used as part of a multi-measurement method which will allow monitoring of the key metabolic changes accompanying neuronal activation. This method will be

used to clarify the mechanism underlying the widely-employed BOLD signal and will have important clinical applications such as the diagnosis and treatment of stroke.

Bibliography

[1] F Bloch. Nuclear induction. *Physical Review*, 70:460-473, 1946.

[2] EM Purcell, HC Torrey, and RV Pound. Resonance absorption by nuclear magnetic moments in a solid. *Physical Review*, 69:37-38, 1946.

[3] A Abragam. *Principles of Nuclear Magnetism*. New York: Oxford University Press, 1961.

[4] R Freeman. *A Handbook of Nuclear Magnetic Resonance*. New York: John Wiley & Sons, 1988.

[5] FW Wehrli. *Basic Priciples of MR Imaging*. Milwaukee: GE Medical Systems Primer, 1988.

[6] DG Nishimura. *Principles of Magnetic Resonance Imaging*. Stanford University Course Notes, 1996.

[7] P Mansfield. Multi-planar image formation using NMR spin echoes. *Journal of Physics*, C10:L55-L58, 1977.

[8] YL Yamamoto, CJ Thompson, M Diksic, and E Meyer. Positron emission tomography. *Radiation, Physics and Chemistry*, 24(3):385-403, 1984.

[9] JW Belliveau, DN Kennedy Jr., RC McKinstry, BR Buchbinder, RM Weisskoff, MS Cohen, JM Vevea, TJ Brady, and BR Rosen. Functional mapping of the human visual cortex by magnetic resonance imaging. *Science*, 254:716-719, 1991.

[10] S Ogawa, DW Tank, R Menon, JM Ellermann, SG Kim, H Merkle, and K Ugurbil. Intrinsic signal changes accompanying sensory stimulation: Functional brain mapping with magnetic resonance imaging. *Proceedings of the National Academy of Sciences of the United States of America*, 89:5951-5955, 1992.

[11] GA Wright, BS Hu, and A Macovski. Estimating oxygen saturation of blood in vivo with MR imaging at 1.5T. *Journal of Magnetic Resonance Imaging*, 1(3):275-284, 1991.

[12] M Jueptner and C Weiller. Review: Does measurement of regional cerebral blood flow reflect synaptic activity? – Implications for PET and fMRI. *Neuroimage*, 2:148-156, 1995.

[13] RD Hoge and GB Pike. Oxidative metabolism and the detection of neuronal activation via imaging. *Journal of Chemical Neuroanatomy*, 22:43-52, 2001.

[14] C Roy and C Sherrington. On the regulation of the blood supply of the brain. *Journal of Physiology*, 11:85-105, 1890.

[15] P Fox, M Mintun, M Raichle, F Miezin, J Allman, and D Van Essen. Mapping human visual cortex with positron emission tomography. *Nature*, 323:806-809, 1986.

[16] RD Hoge, J Atkinson, B Gill, GR Crelier, S Marrett, and GB Pike. Linear coupling between cerebral blood flow and oxygen consumption in activated human cortex. *Proceedings of the National Academy of Sciences of the United States of America*, 96:9403-9408, 1999.

[17] RD Hoge, J Atkinson, B Gill, GR Crelier, S Marrett, and GB Pike. Investigation of BOLD signal dependence on cerebral blood flow and oxygen consumption: The deoxyhemoglobin dilution model. *Magnetic Resonance in Medicine*, 42:849-863, 1999.

[18] CTW Moonen and PA Bandettini (Eds.) *Functional MRI.* New York: Springer-Verlag Berlin Heidelberg, 1999.

[19] EL Barbier, L Lamalle, and M Decorps. Methodology of brain perfusion imaging. *Journal of Magnetic Resonance Imaging*, 13:496-520, 2001.

[20] JA Detre, LS Leigh, DS Williams, and AP Koretsky. Perfusion imaging. *Magnetic Resonance in Medicine*, 23:37-45, 1992.

[21] DS Williams, JA Detre, JS Leigh, and AP Koretsky. Magnetic resonance imaging of perfusion using spin-inversion of arterial water. *Proceedings of the National Academy of Sciences of the United States of America*, 89:212-216, 1992.

[22] SD Wolff and RS Balaban. Magnetization transfer contrast (MTC) and tissue water proton relaxation in vivo. *Magnetic Resonance in Medicine*, 10:135-144, 1989.

[23] HN Yeung and SD Swanson. Transient decay of longitudinal magnetization in heterogeneous spin systems under selective saturation. *Journal of Magnetic Resonance*, 99:466-479, 1992.

[24] RR Edelman, B Siewert, DG Darby, V Thangaraj, AC Nobre, MM Mesulam, and S Warach. Qualitative mapping of cerebral blood flow and functional localization with echo-planar MR imaging and signal targeting with alternating radio frequency. *Radiology*, 192:513-520, 1994.

[25] KK Kwong, DA Chesler, RM Weisskoff, KM Donahue, TL Davis, L Ostergaard, TA Campbell, and BR Rosen. MR perfusion studies with T1-weighted echo planar imaging. *Magnetic Resonance in Medicine*, 34:878-887, 1995.

[26] S-G Kim. Quantification of relative cerebral blood flow change by flow-sensitive alternating inversion recovery (FAIR) technique: Application to functional mapping. *Magnetic Resonance in Medicine*, 34:293-301, 1995.

[27] EC Wong, RB Buxton, and LR Frank. Implementation of quantitative perfusion imaging techniques for functional brain mapping using pulsed arterial spin labeling. *NMR in Biomedicine*, 10:237-249, 1997.

[28] F Calamante, SR Williams, N van Bruggen, KK Kwong, and R Turner. A model for quantification of perfusion in pulsed labelling techniques. *NMR in Biomedicine*, 9:79-83, 1996.

[29] RB Buxton, LR Frank, EC Wong, B Siewert, S Warach, and RR Edelman. A general kinetic model for quantitative perfusion imaging with arterial spin labeling. *Magnetic Resonance in Medicine*, 40:383-396, 1998.

[30] DC Alsop and JA Detre. Reduced transit-time sensitivity in noninvasive magnetic resonance imaging of human cerebral blood flow. *Journal of Cerebral Blood Flow Metabolism*, 16:1236-1249, 1996.

[31] FQ Ye, VS Matay, P Jezzard, JA Frank, DR Weinberger, and AC McLaughlin. Correction for vascular artifacts in cerebral blood flow values measured by using arterial spin tagging techniques. *Magnetic Resonance in Medicine*, 37:226-235, 1997.

[32] EC Wong, RB Buxton, and LR Frank. A theoretical and experimental comparison of continuous and pulsed arterial spin labelling techniques for quantitative perfusion imaging. *Magnetic Resonance in Medicine*, 40:348-355, 1998.

[33] Y Yang, W Engelien, S Xu, H Gu, DA Silbersweig, and E Stern. Transit time, trailing time, and cerebral blood flow during brain activation: Measurement using multislice, pulsed spin-labelling perfusion imaging. *Magnetic Resonance in Medicine*, 44:680-685, 2000.

[34] S-G Kim and NV Tsekos. Perfusion imaging by a flow-sensitive alternating inversion recovery (FAIR) technique: Application to functional brain imaging. *Magnetic Resonance in Medicine*, 37:425-435, 1997.

[35] EC Wong, RB Buxton, and LR Frank. Quantitative imaging of perfusion using a single subtraction (QUIPSS and QUIPSS II). *Magnetic Resonance in Medicine*, 39:702-708, 1998.

[36] MS Silver, RI Joseph, and DI Hoult. Selective spin inversion in nuclear magnetic resonance and coherent optics through an exact solution of the Bloch-Riccati equation. *Physics Review A*, 31:2753-2755, 1985.

[37] W-M Luh, EC Wong, PA Bandettini, and JS Hyde. QUIPSS II with thin-slice TI_1 periodic saturation: A method for improving the accuracy of quantitative perfusion imaging using pulsed arterial spin labeling. *Magnetic Resonance in Medicine*, 41:1246-1254, 1999.

[38] LR Frank, EC Wong, and RB Buxton. Slice profile effects in adiabatic inversion: Application to multislice perfusion imaging. *Magnetic Resonance in Medicine*, 38:558-564, 1997.

[39] GS Payne and MO Leach. Threshold voltages for hyperbolic secant inversion pulses. *NMR in Biomedicine*, 5:142-144, 1992.

[40] GS Payne and MO Leach. Implementation and evaluation of frequency offset corrected inversion (FOCI) pulses on a clinical MR system. *Magnetic Resonance in Medicine*, 38:828-833, 1997.

[41] J Pauly, P Le Roux, D Nishimura, and A Macovski. Parameter relations for the Shinnar-Le Roux selective excitation pulse design algorithm. *IEEE Transactions on Medical Imaging*, 10:53-65, 1991.

[42] I Rock (Ed.) *The Perceptual World*. New York: W.H. Freeman and Company, 1990.

[43] R Hoge. GLstim: An OpenGL based stimulus presentation program for functional MRI. http://www.bic.mni.mcgill.ca/users/rhoge/GLstim/GLstim.html.

[44] P Neelin, D MacDonald, DL Collins, and AC Evans. The MINC file format: From bytes to brains. *Proceedings of the 4th International Conference on Human Brain Mapping*, Montreal, 1998.

[45] KJ Worsley, S Marrett, P Neelin, AC Vandal, KJ Friston, and AC Evans. A united statistical approach for determining significant signals in images of cerebral activation. *Human Brain Mapping*, 4:58-73, 1996.

[46] Y Yang, JA Frank, L Hou, FQ Ye, AC McLaughlin, and JH Duyn. Multi-slice imaging of quantitative cerebral perfusion with pulsed arterial spin labeling. *Magnetic Resonance in Medicine*, 39:825-832, 1998.

[47] WG Schreiber, FJ Guckel, P Stritzke, P Schmiedek, A Schwartz, and G Brix. Cerebral blood flow and cerebrovascular reserve capacity: Estimation by dynamic magnetic resonance imaging. *Journal of Cerebral Blood Flow and Metabolism*, 18:1143-1156, 1998.

[48] FQ Ye, KF Berman, T Ellmore, G Esposito, JD van Horn, Y Yang, J Duyn, AM Smith, JA Frank, DR Weinberger, and AC McLaughlin. $H_2{}^{15}O$ PET validation of steady-state arterial spin tagging cerebral blood flow measurements in humans. *Magnetic Resonance in Medicine*, 44:450-456, 2000.

[49] F Calamante, DL Thomas, GS Pell, J Wiersma, and R Turner. Measuring cerebral blood flow using magnetic resonance imaging techniques. *Journal of Cerebral Blood Flow and Metabolism*, 19:701-735, 1999.

[50] FJ Guckel, G Brix, P Schmiedek, A Piepgras, G Becker, and J Kopke. Cerebrovascular reserve capacity in patients with occlusive cerebrovascular disease: Assessment with dynamic susceptibility contrast-enhanced MR imaging and the acetaxolamide stimulation test. *Radiology*, 201:405-412, 1996.

[51] H Yonas, JM Darby, EC Marks, SR Durham, and C Maxwell. CBF measured by XE-CT: Approach to analysis and normal values. *Journal of Cerebral Blood Flow and Metabolism*, 11:716-725, 1991.

[52] KL Leenders, D Perani, AA Lammerstsma, JD Heather, P Buckingham, JR Healy, JM Gibbs, RJS Wise, Y Hatazawa, S Herold, RP Beany, DJ Brooks, T Spinks, G Rhodes, RSJ Fracowiak, and T Jones. Cerebral blood flow, blood volume, and oxygen utilization: Normal values and effects of age. *Brain*, 113:27-47, 1990.

[53] AJ Martin, KJ Friston, JG Colebatch, and RS Frackowiak. Decreases in regional cerebral blood flow with normal aging. *Journal of Cerebral Blood Flow and Metabolism*, 11:684-689, 1991.

[54] NA Lassen. Normal average value of cerebral blood flow in younger adults is 50 mL/100g/min. *Journal of Cerebral Blood Flow and Metabolism* (Editorial), 5:347-349, 1985.

[55] RD Hoge, J Atkinson, B Gill, GR Crelier, S Marrett, and GB Pike. Stimulus-dependent BOLD and perfusion dynamics in human V1. *NeuroImage*, 9:573-585, 1999.

[56] JS Gati, RS Menon, K Ugurbil, and BK Rutt. Experimental determination of the BOLD field strength dependence in vessels and tissue. *Magnetic Resonance in Medicine*, 38:296-302, 1997.

[57] X-H Zhu, S-G Kim, P Andersen, S Ogawa, K Ugurbil, and W Chen. Simultaneous oxygenation and perfusion imaging study of functional activity in primary visual cortex at different visual stimulation frequency: Quantitative correlation between BOLD and CBF changes. *Magnetic Resonance in Medicine*, 40:703-711, 1998.

[58] W-M Luh, EC Wong, PA Bandettini, BD Ward, and JS Hyde. Comparison of simultaneously measured perfusion and BOLD signal increases during brain activation with T1-based tissue identification. *Magnetic Resonance in Medicine*, 44:137-143, 2000.